High-Efficiency High Power Density Direct Carbon Fuel Cell

A Thesis
Submitted to
WORCESTER POLYTECHNIC INSTITUTE
In partial fulfillment of the requirements for the
Degree of Master of Science
in
Materials Science and Engineering
by
Christian Faria

May 2021

Advisor:
Professor Adam Powell

Committee:
Boyd Davis
Professor Uday Pal
Professor Yu Zhong

Abstract

For over 80 years, combustion turbines have been the preferred method of generating power in excess of 10MW. In addition to producing heat and power, the combustion of fossil fuels releases pollutants in the form volatile organic compounds, oxides of carbon, nitrogen, and sulfur, and fine particulates. Simple cycle (SC) combustion turbines are limited by Carnot efficiency, resulting in thermal efficiencies of 34-39% with the most modern ultra-supercritical plants approaching 50%. By 2040, global electricity demand is projected to increase 57% from its current level, with renewables accounting for only 37% of electricity generation. Increasing electricity demand coupled with stringent emissions regulations drives the need for a more efficient way of generating dispatchable power from carbon-based fuels.

Fuel cells are electrochemical devices that continuously convert the energy from a chemical reaction into electricity. The use of solid carbon fuel allows for separation of reactant and product streams allowing nearly 100% fuel utilization, while low reaction entropy permits high theoretical efficiency. Pure CO_2 gas produced can be captured for sequestration or use in downstream applications. Practical direct carbon fuel cell (DCFC) efficiency is projected to be more than 70%, leading to nearly a 50% reduction in emissions from power generation relative to SC turbines. Prior DCFC designs have suffered from slow transport of reactants to the electrolyte and formation of corrosive compounds resulting in material degradation, short cell lifetime, and power densities less than 1 W/cm^2.

A high-efficiency high power density DCFC is proposed which uses a cathode-supported solid oxide electrolyte such as yttria-stabilized zirconia and an iron and/or manganese based liquid anode alloy with high carbon solubility. Solid fuel containing carbon is submerged and dissolved in the anode, with impurities accumulating in a slag layer at the top of the feed reservoir. Anode reaction kinetics are rapid due to carbon solubility and gas lift stirring. Calculation of Phase Diagrams (CALPHAD) methodology is used to select an alloy composition that has the best combination of low liquidus temperature and high carbon solubility. Mass and energy balance models forecasting operation at 10 bar show this DCFC achieving 40% efficiency at 1000°C with a power density of 5 W/cm^2, and 66% efficiency at 800°C with a power density of 1.37 W/cm^2. Model open-circuit voltage estimates are validated by experiments at various temperatures and with several anode alloy compositions, with empirical results compared to previous works.

This thesis contains an in-depth investigation of the anode alloy development, selection, characterization, and experimentation in a proof-of-concept DCFC apparatus. Models for cost, energy, and net emissions for various types of coal and biomass fuel are compared to conventional methods of power generation. Measurements and data from this research will be contributed to open literature, advancing the future of DCFC technology.

Acknowledgements

I would like to acknowledge my advisor Professor Adam Powell of Worcester Polytechnic Institute (WPI) whose guidance and advice allowed me to conduct the scientific investigation outlined in this thesis. A sincere thank you is extended to my thesis committee members: Boyd Davis, Professor Uday Pal, and Professor Yu Zhong who took the time to review this thesis and provided valuable input during the progression of this research.

Being a member of the Energy Metals Research Group (EMRG) during my time at WPI has improved my ability as researcher and engineer. The EMRG's mission, applying principles of chemistry and engineering to develop innovative sustainable energy processes, will continue to be a source of inspiration. I acknowledge all the EMRG members for their efforts in this pursuit, and specifically Adiyta Moudgal, Hongyi Sun, and Steven Jacek who were always willing to lend a hand in support of this research. Also included is Haoxuan Yan for helping obtain measurements using equipment unavailable at WPI.

Thanks are extended to my friends for their unwavering support and encouragement throughout the challenges faced during my time as a graduate student, and reminding me that the journey is often more important than the destination. I thank my employer whose financial support allowed me to pursue higher education, along with my co-workers in the corporate engineering group whose patience and understanding permitted many adjustments in my schedule required to achieve this work.

Finally, I thank my parents for teaching the importance of curiosity, generosity, and hard work to dream and achieve new goals during each chapter of my life. Thank you to my brother Jay, his wife Ellen, and their son Russell for being a source of light and positivity. Their constant enthusiasm and support towards my endeavors cannot be overstated.

Contents

List of Figures

List of Tables

1. Introduction

Global energy consumption has doubled in the last 25 years, reaching a new record of approximately 14500 million tons oil equivalent (Mtoe) last year (Dong et al, 2020). While this increase in energy availability has greatly contributed to social and economic development across the world, the primary source of energy generation comes from the combustion of carbon-based fossil fuels which adversely affects the environment (Sinha et al. 2017).

1.1 Energy Forecast

In 2018, oil, natural gas, and coal fuels were responsible for generating 64% of the global electricity produced. The remainder of electricity production came from nuclear power, renewable energy sources (RES) and other methods (BP, 2020). Widespread use of RES will significantly reduce global carbon dioxide (CO_2) emissions, however current RES installations make up only 28% of the total electricity generation worldwide. Recent studies forecast the global share of electricity produced by RES, inclusive of hydroelectric, wind, solar, and geothermal power generation methods, will be about 37% by the year 2040 (Ahmad and Zhang, 2020). At that time, a 57% increase in global electricity demand is forecasted, meaning that nuclear power and electricity generation by fossil fuels will still be large contributors to the total amount of electricity produced.

1.2 Conventional Methods of Power Generation

For over 80 years, combustion turbines have been the preferred heat engines used to generate power in quantities over 10 MW (Lindeburg, 2020). In these devices, heat from the combustion fuel and air is used to perform work required to produce electricity as shown in a simple cycle (SC) combustion turbine in **figure 1**. To achieve continuous operation, a series of processes occur that convert input energy to useful output work. The efficiency, η, of a power cycle is shown mathematically below.

$$\eta = \frac{net\ work\ output}{energy\ input} = \frac{W_{net}}{Q_{in}} \qquad [1]$$

The maximum efficiency of a heat engine was first investigated by Sadi Carnot in the early 19th century to understand the maximum efficiency of heat engines used in industrial processes. The Carnot cycle, in terms of the second law of thermodynamics, states that the maximum efficiency of a reversible cyclical process occurs when there is no change in entropy. The Carnot cycle can be visualized in **figure 2**.

$$\Delta s \geq \int_{T_1}^{T_2} \frac{dq}{T} \qquad [2]$$

In 1850 Rudolph Clausius conducted experiments to prove that whenever work is done by heat, an equivalent amount of heat is consumed (O'Connor and Robertson, 2000). This was the basis for the First Law of Thermodynamics, stating that the total energy of an isolated system is constant and different types of energy (heat and work) can be converted from one form to another but cannot be created or destroyed.

In terms of a power cycle, the first law can be written as:

$$Q_{in} = Q_{out} + W_{net} \qquad [3]$$

Combining equations [1] and [3] allows the thermal efficiency of a power cycle to be expressed in terms of heat:

$$\eta = \frac{Q_{in} - Q_{out}}{Q_{in}} \qquad [4]$$

Therefore 100% efficiency can only occur when Q_{out}, heat energy lost to the environment, is zero. If this was to occur the process would have no change in entropy and the cycle would be reversible. Considering frictional losses present in all mechanical devices, such a process is impossible. All real-world processes starting in one equilibrium state and ending in another occur in the direction that causes entropy of the system and environment to increase (Lindeburg, 2020). This can also be visualized in terms of the ratio of absolute temperatures of the engine's heat reservoirs, which Carnot determined was proportional to the ratio of heat transfer:

$$\eta = \frac{T_H - T_L}{T_H} \qquad [5]$$

To achieve 100% efficiency, all heat from the high temperature reservoir would have to be converted into work, meaning the low temperature reservoir would need to be absolute zero, which is not attainable in a real-world device. High temperature values are dictated by materials selection, and despite advances in the field, approach their limit around 1290°C (Lindberg, 2020). Maximum real-world efficiency is achieved when low temperature reservoir is equal to ambient conditions. Using 1260°C and 20°C for T_H and T_L respectively, maximum thermal efficiency is about 80%. This does not consider losses due to bearing friction, turbulence, or incomplete combustion.

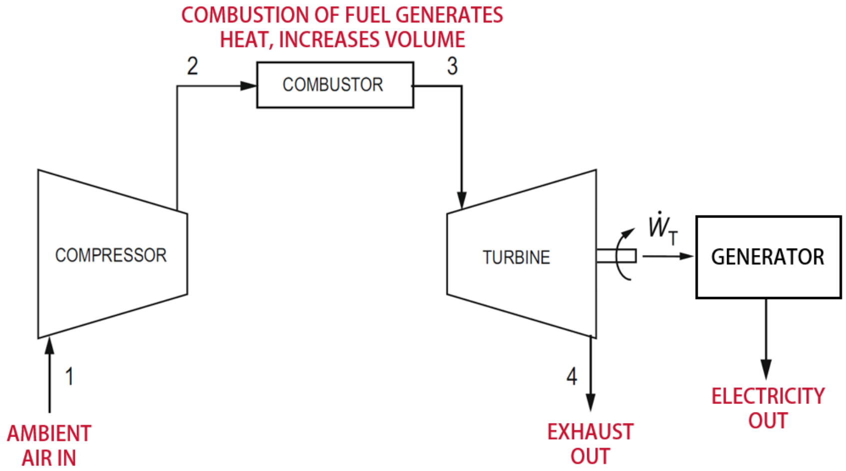

Figure 1: In a combustion turbine, a range of gaseous and distillate fuels are mixed with air then ignited to produce high-pressure gas that expands as it is directed through a turbine, whose subsequent rotation is used to produce shaft power for an electric generator (Sirignano and Liu, 1999) (Lindeburg, 2020).

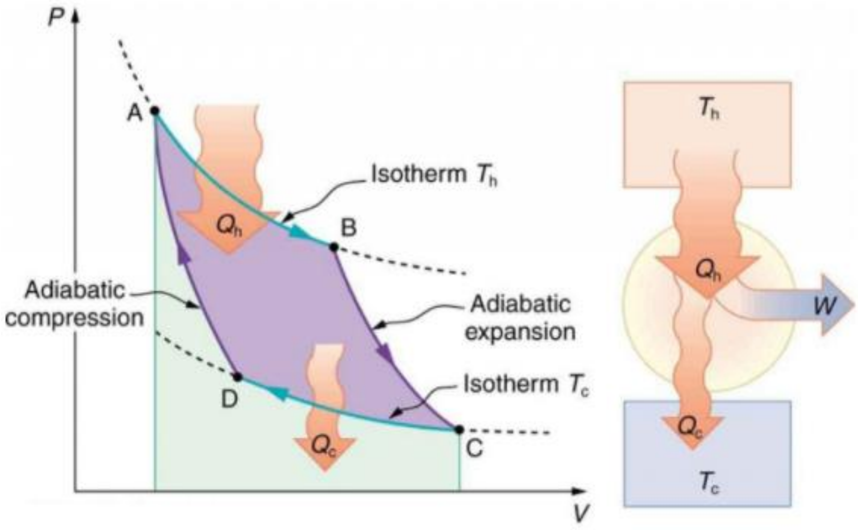

Figure 2: The Carnot cycle (Balmer, 2011).

Gas turbines can either be powered directly by combustion products flowing through the turbine, or indirectly by using another working fluid, such as steam, to rotate the turbine and subsequent generator. Using combustion gases directly results in higher turbine efficiencies due to the absence of losses through a heat exchanger, however exposure to exhaust gases deteriorates turbine components at a faster rate. Modern SC direct combustion turbines operate with a maximum thermal efficiency of about 39%. Overall plant efficiency can be improved by using the high temperature exhaust gases from one indirect turbine to provide a portion of the heat needed to create steam for a second turbine. These combined cycle installations are capable of 64% total efficiency (GE, 2017). It normally takes 10 years of development to raise turbine power plant efficiency levels by 1% (GE, 2016).

In addition to relatively low efficiencies, gas turbines result in the depletion of natural resources and generation of pollutants (Sinha et al., 2017). Primarily, carbon dioxide (CO_2) and water vapor is produced during the combustion process, with nitrogen oxides (NO_x), sulfur oxides (SO_x), volatile organic compounds (VOCs), and fine particulates also present in the exhaust gas stream.

National standards for regulating emissions from stationary sources were put in place by Japan in the early 1960s, followed by the United States introducing the Clean Air Act in 1963. Emissions regulations in parts of Europe were instituted in 1974, and subsequent countries including Brazil, India, and China established their own emissions regulations in the 1990s (Johnstone et al., 2017). These standards defined a threshold of pollutants in the form of fine particulates, sulfur oxides (SO_x) and nitrogen dioxide (NO_2) that could be released per unit volume of exhaust gases, based on parameters like plant size in megawatts of thermal input (MWt) and fuel type used. In more recent decades, intergovernmental organizations, such as the International Energy Agency (IEA) began to serve as advisors to emerging economies, guiding them to pursue cleaner methods of energy generation with many countries and companies setting a benchmark of net zero emissions by 2050 (Green & Ekblom, 2018).

In response to increasing pressure to reduce CO_2 emissions, some powerplants have implemented systems downstream of their gas turbines for carbon capture and sequestration (CCS). A plant using CCS with combustion turbines must be capable of separating CO_2 from the exhaust stream containing pure elements in air and pollutants from the combustion process. This adds immense complexity and cost to power generation processes, with additional energy penalties that decrease system efficiency (Giddey et al., 2012). To mitigate these negative aspects of CCS, some combustion turbines operate on pure oxygen, rather than air. This results in an exhaust gas stream consisting of mainly CO_2 and water vapor, from which CO_2 is easier to separate.

As shown in **figure 3**, the CO_2 collected during the CCS process is compressed and transported to deep (often more than one mile) underground rock formations where the gas is trapped, preventing its escape into the atmosphere (EPA, 2017). Despite the reduction of emissions from CCS, it has not seen widespread use due to high costs and a lack of regulatory framework (Nanda et al., 2016). Currently, less than 1% of annual CO_2 emissions are captured for sequestration (Gonzales et al. 2020).

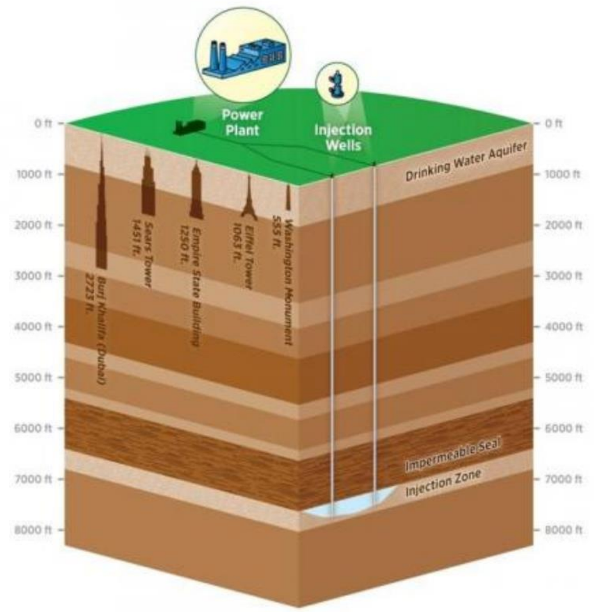

Figure 3: CCS Diagram with depth shown to scale (EPA, 2017).

1.3 Generation from Renewable Resources

Renewable resources, such as solar, thermal, wind, or hydro power are attractive alternatives to conventional methods because they generate electricity from processes from continually occurring natural processes that are replenished much faster than fossil fuels. The United States has seen strong growth in the renewable energy sector over the past 15 years, with this increase forecasted to accelerate over the next decade due to the influence of global organizations stressing the need for climate change mitigation (Outka, 2021).

However, power generation by renewable sources is subject to environmental conditions, and therefore intermittent by nature. The output of a solar cell is a function of the sun's angle on the panel, while power generation by wind turbines depends on amount of kinetic energy delivered by moving air. Wind power varies as the cube of instantaneous wind speed, resulting in higher variations in power output than in wind velocity (Hoste, 2020). A study by Hoste et al. 2020 revealed maximum generation by solar panels in California between 10am and 4pm, while wind power reached its daily height in the early evening. Overlaying these values on a plot for daily demand for electricity shows that most of the power generated by renewables occurs when the demand is low. Currently peak demand is satisfied by combustion turbines, but as generation shifts more towards renewable sources, there exists a need for an efficient method of power generation that can work intermittently with renewables to satisfy peak demand during the morning and evening hours.

1.4 What is a Fuel Cell?

A fuel cell is a device that converts energy from a chemical reaction to electrical and thermal energy, and as such is referred to as an electrochemical cell. Fuel cells can operate continuously so long as an adequate supply of fuel and oxidizer is present, and their operation is far more simple than conventional power generation methods such as turbines or reciprocating engines, resulting in nearly silent operation. Furthermore, since power is produced via chemical reaction rather than combustion, fuel cells have high energy efficiency dictated by the reaction taking place, and products of the reaction can be readily captured for use or sequestration. Their modular nature allows for units to range in size from several hundred kilowatts to tens of megawatts without efficiency penalties, making them well-suited for centralized large-scale generation and smaller distributed applications alike (Giddey et al., 2012).

The first demonstration of a fuel cell is credited to Grove in 1839 in a device he had constructed to study the electrolysis of water (Grove, 1839). He found that when the current was turned off, there was a small current that flowed in the opposite direction, resulting from the hydrogen and oxygen in the system reacting to form H_2O. He postulated that a series of these devices could be connected to create a voltaic battery and observed that a 'notable surface of action' was required between the gas, electrolyte, and electrode phases in a cell (Stolten, 2010).

The basic components of Grove's apparatus are shared by all fuel cells and are visualized in **figure 4**. A fuel cell consists of two porous electrodes: the anode and the cathode, which allow fuel and oxidizer to be continually introduced. These two electrodes are connected by an ion-conducting electrolyte, facilitating interaction of reactants within the cell. Fuel and oxygen pass through the electrolyte as ions, moving from regions of high concentration in the electrodes to lower concentration in the electrolyte due to the electrochemical reaction taking place, turning the reactant species into molecules. Current enters the cell at the anode and leaves at the cathode, with electrons exchanged during the chemical reaction flowing opposite to the direction of current flow. Since the electrolyte is the intermediary between the anode and cathode, the speed at which reactants can be transported, or diffused, through this material governs the rate of the chemical reaction and subsequent electricity produced. For this reason, fuel cells are usually classified by their electrolyte material.

Fuel cell performance is classified by overall efficiency and power density [W/unit area] of the electrolyte. Overall efficiency the actual cell voltage divided by the theoretical (i.e. without any losses) voltage of the reaction, while power density is the product of cell voltage and current density. The method in which these values are calculated is detailed in section 4.2.

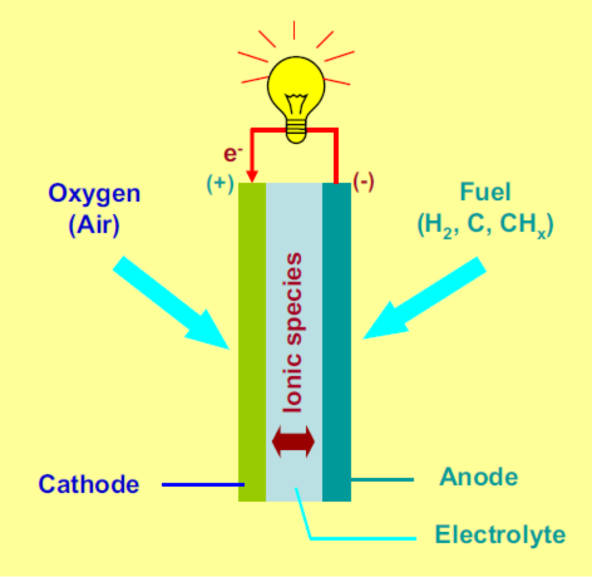

Figure 4: Basic components of a fuel cell (Giddey et al., 2012).

1.5 DCFC Overview

A direct carbon fuel cell utilizes the energy produced from the reaction between solid carbon and oxygen gas. The cell reaction is:

$$C + O_2 \rightarrow CO_2 \qquad [6]$$

Since the change in entropy of this reaction is close to zero, theoretical efficiency is nearly 100%. The half-cell (those occurring at the cathode and anode) reactions are:

$$Cathode: \quad O_2 + 4e^- \rightarrow 2O^{2-} \qquad [7]$$
$$Anode: \quad 2O^{2-} + C \ \rightarrow CO_2 + 4e^- \qquad [8]$$

In a fuel cell, electricity is captured from the chemical reaction taking place, rather than relying on pressure and thermal gradients to drive rotary components as in a heat engine. The design is referred to as ‘direct’ since solid carbon fuel can be used in the device rather than converting it to a gaseous phase prior to introduction which is typical for conventional power generation methods. This simplifies process flow, and DCFC installation costs are generally lower than conventional turbines (Giddey et al., 2012). The ability to operate the cell on solid carbon allows for a wide variety of fuel sources, including biomass, polymers, and traditional fossil fuels with minimal reforming before introduction to the device. In addition, the reaction product is exhausted in a pure gas stream, rather than being mixed with other pollutants as found in SC turbines.

1.6 Thesis Outline

This thesis investigates previous DCFC designs and examines the viability of a liquid anode for use in a novel DCFC design. Chapter 3 explains the design philosophy and method used to determine candidate materials for the anode. Chapter 4 shows equations used to create performance models of this DCFC, projecting overall efficiency and power density of the device. Chapter 5 describes the experimental apparatus used to test different anode compositions, with the results presented. Chapter 6 discusses the results and their impact on the design, followed by the conclusion in Chapter 7 where future work is proposed.

2. Related Works

The first electrochemical cell using solid carbon as a fuel was demonstrated by William Jacques in 1896. In this design, shown in **figure 5**, he used a molten hydroxide electrolyte, specifically caustic soda (NaOH), with a fuel rod made from coal which functioned also functioned as the anode. An iron vessel containing the NaOH electrolyte functioned as the cathode, with air being blown in under the electrolyte surface to combine with carbon in the coal fuel rod to create carbon dioxide. In connecting 100 of these cells, Jacques was able to produce over 1kW of power, however the reaction led to the formation of carbonate within the electrolyte which hindered the electrolyte's effectiveness and aggressively corroded the cell components. Furthermore, impurities in the carbon fuel rod dissolving into the electrolyte reduced its efficiency. While the contaminated electrolyte could be periodically removed and refilled with new molten sodium hydroxide, the degradation of metallic materials within the cell from carbonate formation could not be avoided and hindered the device from commercial use.

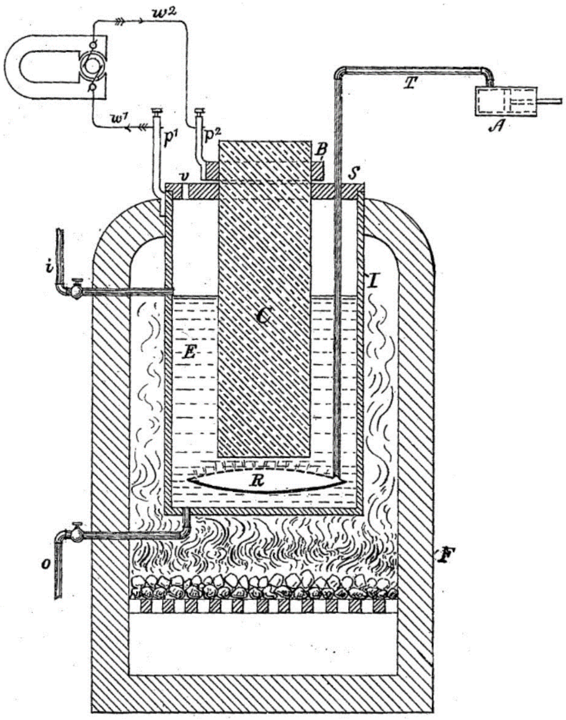

Figure 5: Schematic of the first documented DCFC by William Jacques. C is the graphite (carbon) fuel rod and anode; I is an iron containment pot functioning and cathode. E is a molten sodium hydrate electrolyte, heated by the furnace, F. Air is introduced to the electrolyte by the pump, A, and distributed through the ring-shaped manifold, R (Jacques, 1896). While the cell did succeed at generating electricity, the formation of carbonate within the electrolyte corroded the cell so quickly that the design was not feasible for commercial applications.

2.1 Types of DCFCs

Despite its short operating time, Jacques' invention proved that electricity could be generated using solid carbon in an electrochemical cell. Throughout the 20th century, researchers have further investigated DCFC geometry and materials of construction in the pursuit of a design that could be viable for commercial applications. Advancements have led to DCFCs using three types of electrolyte: molten hydroxide, molten carbonate, or oxygen-ion conducting ceramic.

2.1.1 Molten Hydroxide

Using sodium hydroxide (NaOH) or potassium hydroxide (KOH) as a DCFC electrolyte material is attractive due to high ionic conductivity, high reactivity towards carbon, and a low melting point (Giddey et al., 2012). The rapid transport of oxygen ions combined with high reactivity towards carbon creates favorable conditions for anodic oxidation and formation of carbon dioxide. With these electrolytes exhibiting melting temperatures just above 300°C, electrochemical cells can operate at relatively low temperatures, between 400°C to 650°C, which eliminates the need for high-temperature materials and allows for favorable cell reactions (Zecevic et al., 2004).

In 2005, Scientific Applications and Research Associates (SARA) Inc. re-visited Jacques' original DCFC design with the benefit of modern engineering materials. Instead of rolled iron, the cathode container was made from low carbon steel lined with nickel foam or Ti-doped mild steel (Patton, 2005). Carbonate formation rate in the electrolyte was reduced by introducing humidified air, which decreases O_2 concentration in the electrolyte (Goret et al., 1967). A porous alumina or perforated nickel foil separator isolated the anode and cathode, preventing the chemical reaction of oxygen with the anode and promoting the desired electrochemical cell reaction (Patton & Zecevic, 2005). These improvements resulted in a cell open-circuit voltage (OCV) of 0.85 V at 600°C with a power density of 50 mA/cm^2 and total lifetime of 540h (Zecevic et al., 2004)

In 2012 researchers at Brown University achieved an OCV measurement over 1 V by reducing parasitic direct chemical (instead of electrochemical) reaction losses of carbon with oxygen. To achieve this, both the anode and cathode were surrounded in a porous nickel mesh submerged in a NaOH/KOH eutectic electrolyte, shown in **figure 6**. The cell showed consistent performance operating at 550°C for over 100 hours, with a maximum power density of 34 mW/cm^2 at 0.5 V (Guo et al., 2013). Low power density was attributed to ohmic losses between the anode and cathode rather than contamination of the electrolyte.

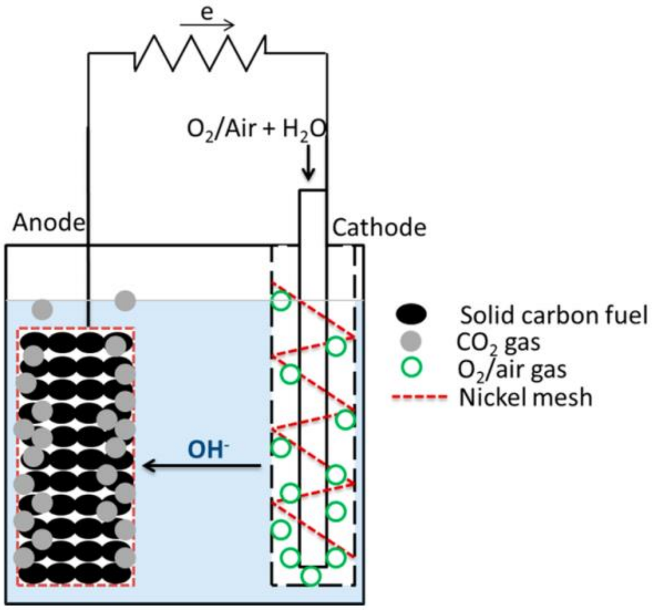

Figure 6: Schematic of molten hydroxide DCFC using nickel mesh to isolate anode and cathode (Guo et al., 2013).

2.2.2 Molten Carbonate

Like molten hydroxide electrolytes, molten carbonate electrolytes exhibit high ionic conductivity. Molten carbonate fuel cells (MCFC) using gaseous fuel, such as natural gas (CH_4), have been adopted for stationary generation of power between 250kW to 1MW at over 100 installations in the U.S. alone (Weidner et al. 2019). Operation with gaseous fuel allows for these devices to be easily integrated with existing infrastructure, and cell efficiency can approach 60% (Kim et al., 2021). While electricity is produced via the reaction of hydrogen with oxygen, carbon plays an important role in these cell types by reforming gaseous fuel and permitting oxygen ion transport across the electrolyte. Using a stack-type design with a lithium, potassium, or sodium carbonate contained within a porous ceramic tape-cast matrix, these fuel cells can achieve power densities between 120-160 mW/cm^2. CH_4 fed into a molten carbonate fuel cell operating between 600°C to 850°C is reformed into carbon monoxide and hydrogen, which react with oxygen in the incoming air stream by the following electrochemical reactions:

$$Anode: \quad H_2 + CO_3^{2-} \rightarrow H_2O + CO_2 + 2e^- \quad [9]$$

$$Cathode: \quad \frac{1}{2}O_2 + CO_2 + 2e^- \rightarrow CO_3^{2-} \quad [10]$$

Cell operating temperature exceeds that of cells using molten hydroxide electrolytes due to the relatively high melting point of carbonates. To improve overall efficiency, heat from the fuel cell stack can be used to produce hot water or steam. Such combined heat and power (CHP) setups are attractive for stationary applications where there is a demand for electricity and thermal energy. **Figure 7** shows a 2.8 MW fuel cell used to provide CHP to part of the University of California at San Diego and is powered by methane from the San Diego municipal waste plant. While cell lifetime exceeds that of types using a molten hydroxide electrolyte, molten carbonate electrolytes experience decreasing effectiveness due to vaporization and coarsening of grains within the ceramic matrix structure (Giddey et al., 2012). Corrosion of cell components coupled with loss of electrolyte efficiency results in a stack life of less than 5 years, after which the stack must be completely disassembled or replaced to install a new electrolyte.

Figure 7: 2.8 MW gas-fed molten carbonate fuel cell at UC San Diego.

Solid carbon can be used to fuel a MCFC by being introduced in the form of fine particles suspended in a slurry. This requires processing of fuel before being added to the cell, however this extra processing step could be justified if the advantages of a molten carbonate electrolyte can be achieved in a DCFC setup. Benefits of using a molten carbonate electrolyte are similar to those of a molten hydroxide electrolyte (high ionic conductivity, low melting point) with improved lifetimes due the addition of sodium carbonate which reduces reactivity of the electrolyte (Tanimoto et al., 1998).

In a molten carbonate DCFC, carbon in the slurry reacts with carbonate ions in the electrolyte, usually consisting of lithium and potassium carbonate mixture, to produce carbon dioxide. Oxygen gas reacts with carbon dioxide to form carbonate through the same reaction that creates carbonate (undesirably) within a molten hydroxide electrolyte. The overall electrochemical cell reaction is identical to [6], but the anode and cathode half-cell reactions are shown below:

$$Anode: \quad C + 2CO_3^{2-} \rightarrow 3CO_2 + 4e^- \tag{11}$$

$$Cathode: \quad O_2 + 2CO_2 + 4e^- \rightarrow 2CO_3^{2-} \tag{12}$$

Adapting the gas fueled MCFC design to work with a carbon fuel slurry, Cherepy et al. measured an OCV of 0.8V at a power density of 96 mW/cm^2. This power density is comparable to that achieved in a gas fueled MCFC, but efficiencies of up to 80% have been realized using solid carbon fuels. Increased efficiency is a result of cell geometry and increased density of reaction sites in the cell using fuel in slurry form (Cherepy et al., 2004).

Recently Kouchachvili et al. tested a continuously fueled molten carbonate planar DCFC operating at 700°C. Nitrogen gas was used to continually deliver powdered carbon fuel to the anode as shown in **figure 8**, but insufficient distribution of the carbon on the anode resulted in an OCV of 0.8V after 3 days of continuous operation but a low power density of 17mW/cm^2. This shows that a planar DCFC using molten carbonate electrolyte can achieve comparable voltage efficiency with continuous fuel delivery.

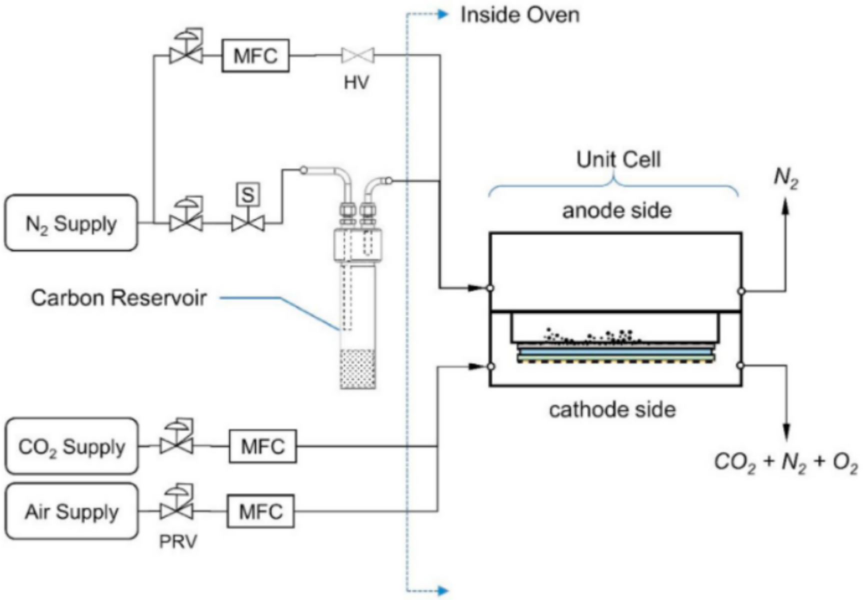

Figure 8: Schematic of continuously fueled planar DCFC using molten carbonate electrolyte. A mass flow controller (MFC) was used to regulate the introduction of reactants (Kouchachvili et al., 2021).

2.2.3 Solid Oxide

A solid oxide fuel cell (SOFC) uses an oxygen-ion conducting ceramic electrolyte to facilitate interaction between the anode and cathode. Zirconia (ZrO_2) is a common electrolyte material due to its high ionic conductivity. However, conductivity at a rate required for electrochemical processes to occur is only attainable at elevated temperatures, requiring fuel cells of this type to operate between 500°C and 1000°C. Fuel cell operation at these temperatures creates a host of challenges, including the implementation of expensive materials that can handle the thermal stresses experienced, increased thermal loss to the environment, and long startup times which can be on the order of several hours. A key benefit of the ceramic electrolyte is it remains chemically inert during operation, avoiding degradation issues experienced by molten hydroxide or carbonate fuel cells (Nürnberger et al., 2009).

At room temperature zirconia is stable in its monoclinic phase, which transitions to tetragonal at 1170°C and cubic at 2370°C. The cubic phase is desired for oxygen ion conduction, and to realize this phase at lower temperatures, 8-9 mol % of yttria is substituted into the cubic fluorite structure. The resulting yttria-stabilized zirconia (YSZ) contains oxygen vacancies, shown in a unit cell in **figure 9**, that facilitate ion transport through the material at elevated temperatures. The high material and processing cost of this electrolyte has presented an obstacle for the commercialization of solid-oxide electrolytes (Gu et al., 2007).

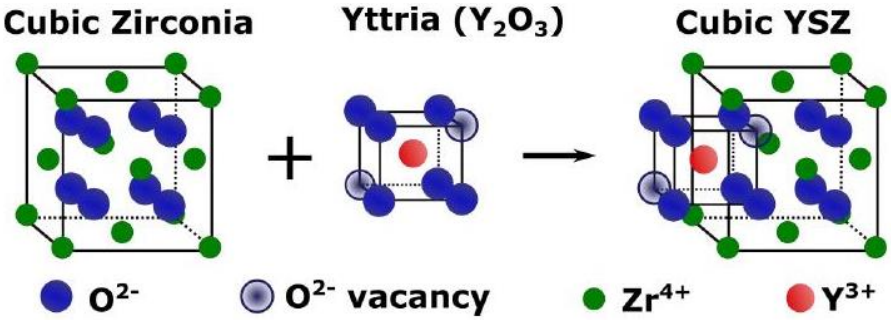

Figure 9: Unit cell of yttria-stabilized zirconia (YSZ) showing vacancy sites allowing for oxygen ion transport (Holz, 2017).

Other materials, such as scandia-stabilized zirconia (ScSZ) or gadolinia-doped ceria (GDC) have also been investigated for use as solid-oxide electrolytes. ScSZ exhibits the highest ionic conductivity of zirconia-based electrolyte materials, however its cost is 2-3 times more expensive per unit mass than yttria (USGS, 2021). Ceria-based electrolytes such as GDC exhibit higher ionic conductivity than YSZ with a lower activation energy for conduction. This allows for lower cell operating temperatures in the range of 700°C (Nürnberger et al., 2009).

2.2.3.1 SOFC with Planar Arrangement

Zevcevic et al. reported that using planar piece of solid carbon in direct contact with a solid oxide electrolyte yields poor cell performance due to gaps at the contact interface from surface irregularities. This is not an issue with molten electrolytes as liquid takes on the shape of its container and contact surfaces with the electrodes.

Using a YSZ electrolyte in the planar DCFC arrangement shown in **figure 10**, Nürnberger et al. tested the effect of differing forms of carbon fuel, carbon black and graphite, on electrochemical cell performance. Their approach to ensuring good surface contact between fuels in pellet form and the solid oxide electrolyte was to use a smaller active contact area, taking advantage of higher fuel density of the solid phase. At 1000°C using carbon black they achieved an OCV of 0.8 V and a power density of 40 mW/cm^2, and 0.45 V with <1 mW/cm^2 using graphite. The authors cited the amorphous structure of carbon black had a lower activation energy (100 kJ/mol) than the crystalline graphite (290 kJ/mol) which improved its reactivity in the cell and thus overall cell performance. Their results showed the scission of carbon bonds was the most important reaction step within the electro-oxidation of carbon (Nürnberger et al., 2009).

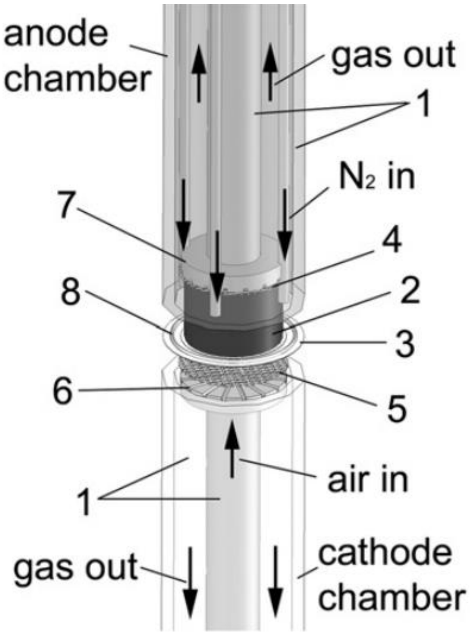

Figure 10: Planar DCFC using a solid oxide electrolyte. The anode and cathode chambers are made from alumina (Al_2O_3) tubes with a 100μm thick YSZ electrolyte (3) between them. Items (4) and (5) are Ni and Pt current collector meshes, respectively, and (6) and (7) are the cathode and anode flow fields which guide reactants to reaction sites. Item (8) is a gold wire used to seal the anode chamber (Nürnberger et al., 2009).

2.2.3.2 SOFC MCFC Hybrid Design

Jiang et al. developed a hybrid DCFC design that incorporates elements of a MCFC with a SOFC to improve overall efficiency. At first glance their design, shown in **figure 11**, looks like that used by Nürnberger et al. but uses a molten carbonate electrolyte consisting of carbon and lithium potassium carbonate in the anode chamber improve contact between the anode and solid oxide electrolyte. The solid oxide electrolyte between the anode and cathode chambers prevents molten carbonate from degrading the cathode, increasing operating time of the cell. Using a NiO anode, and lanthanum-strontium cobaltite (LSC) cathode and a 5μm thick YSZ electrolyte, the cell achieved an OCV of 0.7 V and power density of 878 mW/cm^2 at a temperature of 750°C. The high power density was the result of low ohmic resistance due to extremely thin solid oxide electrolyte, high degree of contact between the anode and electrolyte, and flowing air introduced at the cathode improving diffusion through the solid oxide electrolyte (Jiang et al., 2012). To the author's knowledge this power density holds the current DCFC record.

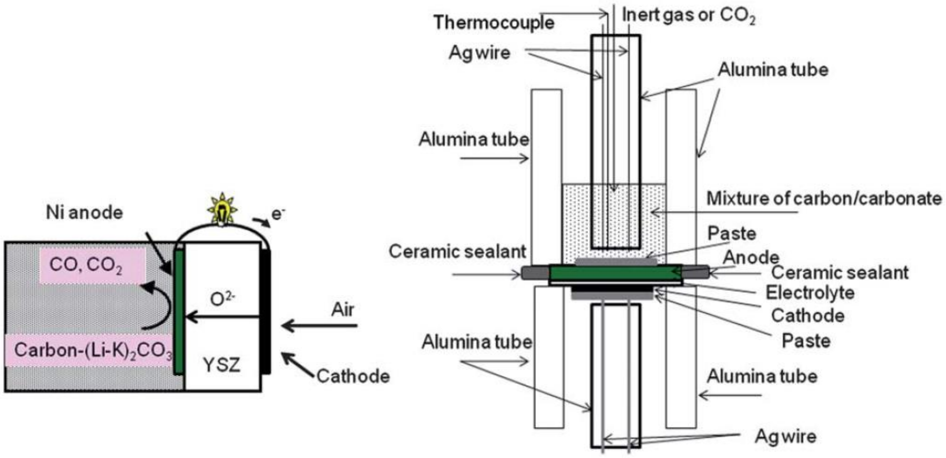

Figure 11: Hybrid DCFC design. This uses a MCFC to ensure sufficient contact between the anode and solid oxide electrolyte (shown in green), while the solid oxide electrolyte separates the carbonate from the cathode chamber, increasing cell lifetime (Jiang et al., 2012).

2.2.3.3 SOFC with Fuel in Liquid Metal

A major obstacle of DCFC implementation is allowing for continuous solid-fuel supply to a single cell (Kouchachvili et al., 2021). Yentekakis et al. proposed a design that used a fused metal anode (FMA) with a solid oxide electrolyte to simultaneously gasify coal and produce electricity. The design, shown in **figure 12**, was only analyzed for macroscopic balance equations, but never assembled or tested. The analysis revealed that electrochemical reactions would take place before the iron FMA reached its liquid state, which the authors disregarded as temperatures below the melting point would not result in coal gasification. Using a pure iron anode, power density was forecasted to be ~100 mW/cm^2 at 1250°C. This does not show any performance increase over existing MCFC or SOFC designs. Furthermore, an electrochemical cell using an Fe-C eutectic composition would need to be operated at a minimum of 1150°C to achieve melting of the metal anode, which would result in high thermal and electrical losses.

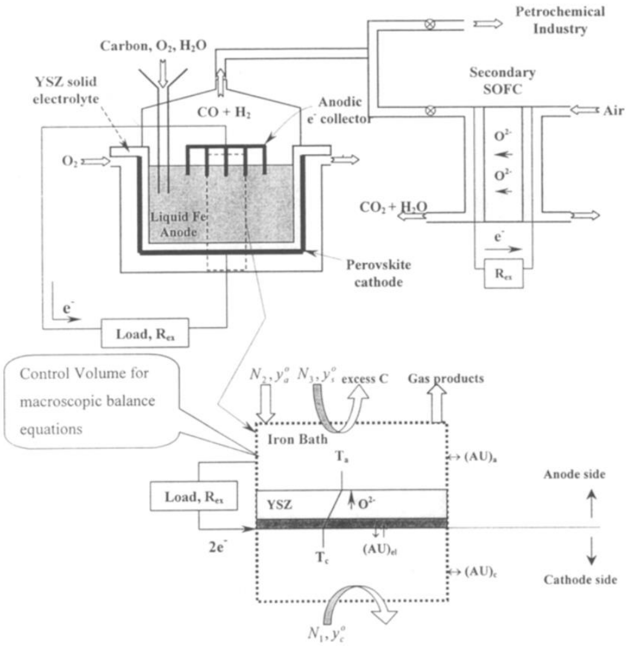

Figure 12: Fused metal anode solid oxide fuel cell proposed by Yentekakis et al. to achieve simultaneous coal gasification and power generation (Yentekakis et al., 1999).

While an Fe-C metal anode would require an operating temperature far higher than what is desired for SOFC designs, other metals could be better suited for a liquid metal anode. In 2010, Jayakumar et al. investigated several metal anodes for use in an SOFC to determine their suitability with a YSZ electrolyte when the cell was in battery mode (i.e. no fuel present). In this mode the metal anode undergoes an oxidation reaction when meeting oxygen ions at the electrolyte surface, which is then reduced once fuel is introduced to the anode, creating CO or CO_2 (Jayakumar et al., 2010).

Tin (Sn), bismuth (Bi), lead (Pb), indium (In), and antimony (Sb) were tested at cell temperatures between 700°C and 800°C in the apparatus shown in **figure 13**. It was found that the SnO_2 oxide layer on the YSZ surface negatively impacted cell performance by impeding oxygen transport to the anode at temperatures up to 800°C. Above 1000°C oxygen ion diffusivity through the SnO_2 increased sufficiently to not hinder cell performance (Tao et al., 2007). The formation of Bi_2O_3 on the YSZ surface did not limit oxygen transport between 700°C and 800°C. Results using In were similar to those of Sn, while Pb showed a decrease in performance when the cell was operated below the melting point of PbO (888°C). Sb showed the best performance, due to the low (656°C) melting point of Sb_2O_3 and reduction of this oxide above 700°C. However, neither Sb nor Pb are desirable for use as molten anodes due to their toxicity (Lagrille, 2013).

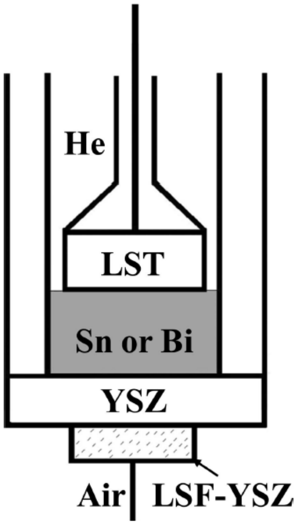

Figure 13: Schematic of experimental apparatus used to test suitability of tin (Sn), bismuth (Bi), lead (Pb), indium (In), and antimony (Sb) metal anodes with a YSZ electrolyte (Jayakumar et al. 2010).

In 2010 Pati investigated the use of a liquid metal anode in a solid oxide membrane electrolyzer to produce hydrogen gas, shown in **figure 14**. A YSZ electrolyte was used with a dip coated Ni-YSZ cathode on one side and liquid metal anode on the other side (Pati, 2010). Steam-rich gas was introduced at the cathode side and carbonaceous fuel was introduced at the liquid metal anode as a reductant to produce hydrogen gas. Tin (Sn), silver (Ag), and copper (Cu) were considered for use as the liquid metal anode. Sn was selected due to its combination of low melting point (232°C) and high boiling point (2602°C). These characteristics allowed for the apparatus to operate within its desired temperature range of 900°C to 1000°C with low volatility of the liquid metal anode. Since Sn has very low solubility of carbon or hydrogen, iron (Fe) was added to the liquid metal anode, increasing carbon and hydrogen solubility within the bulk liquid and the overall reaction zone for electrolytic production of hydrogen. A 4 wt.% Fe-Sn alloy was created for use in the apparatus, which exhibited a liquidus temperature around 900°C. Preliminary results showed that the anodic reaction rate was increased when using this Fe-Sn alloy. It was concluded that further analysis would be required to confirm that an Fe-Sn alloy was a better candidate for the liquid anode rather than Sn alone (Pati, 2010).

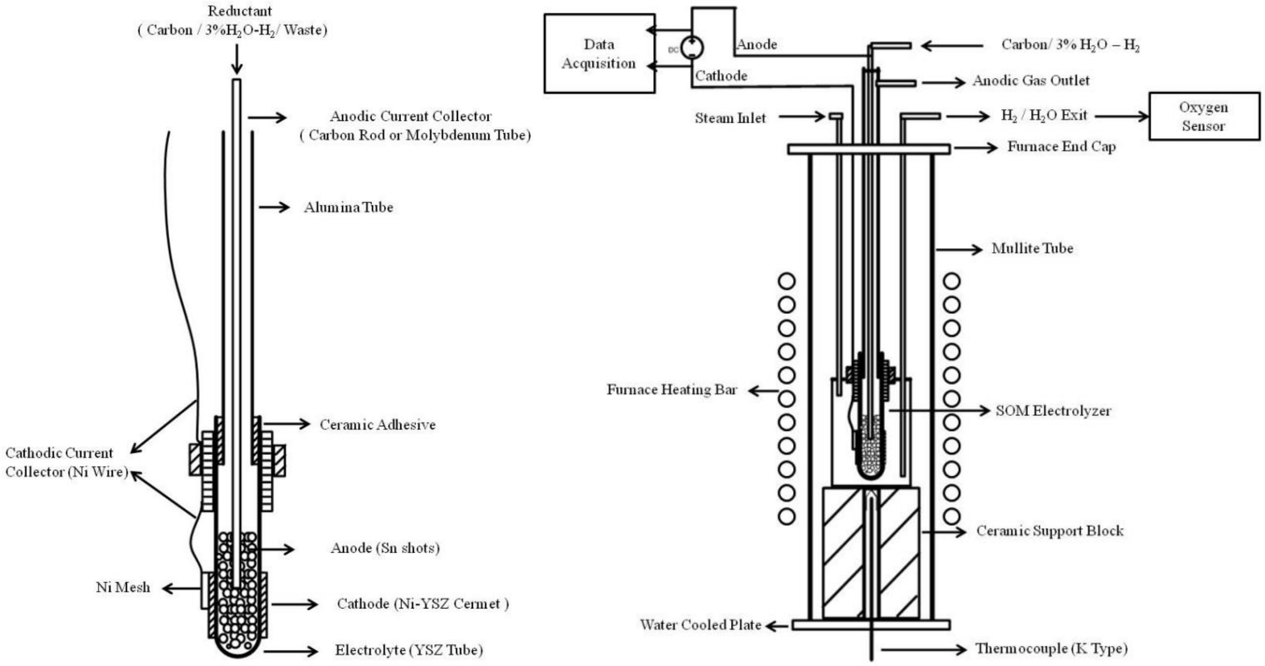

Figure 14: Schematic of (a) laboratory-scale solid oxide membrane electrolyzer and (b) electrolyzer shown in its testing fixture (Pati, 2010).

In 2013 Lagrille analyzed a design by CellTech Power Inc. using molten tin anode with a 200μm thick YSZ electrolyte and lanthanum-strontium magnate (LSM) or lanthanum cobalt manganite (LCM) cathode. Performance was measured running the cell at 900°C in battery mode and fuel cell mode with and without stirring in the anode operating on either kerosene-based jet fuel (JP8) or hydrogen. It was found that SnO_2 buildup on the electrolyte surface was unavoidable at an operating temperature of 900°C, even with stirring induced by hydrogen and helium gas injection. This oxide buildup contributed to a decrease in cell performance after several hours. It was determined that further analysis using different stirring rates and long-term performance trials were required to better understand reaction kinetics in the Sn anode.

3. Methodology

3.1 High-Efficiency High Power Density DCFC Design

The DCFC apparatus explained below was designed by Boyd Davis, Adam Powell, and Uday Pal. Like the design proposed by Yentekakis et al., it combines principles of steelmaking with SOFC technology, using a liquid metal anode to deliver solid carbon fuel to a solid oxide electrolyte. The liquid metal anode proposed is an Fe-based alloy to achieve high carbon solubility and a low enough melting temperature for favorable electrochemical cell operation. Compared to previous work, benefits of using this liquid anode alloy include:

1. Low liquidus (melting) temperature by incorporating alloying elements, resulting in higher efficiency due to production of CO_2 along with CO and lower energy losses
2. High carbon solubility with rapid carbon diffusion
3. High electronic conductivity relative to molten carbonates
4. Compatibility with solid oxide electrolytes and steelmaking refractories

Several cell geometries have been proposed. In **figure 15**, a partial dam separates the fuel feeding section from the electrochemical reaction site. Fuel can be introduced from above by lance or blown in from the side or bottom using a carrier gas, with carbon fuel dissolving into the liquid metal contacting the electrolyte surface. Impurities present within the solid fuel, such as ash and oxides, form a slag layer at the top of the feed section and could be periodically removed. Closed-end cathode tubes with a dip-coated electrolyte layer are submerged in the anode alloy, avoiding leakage between component interfaces often experienced with planar arrangements (Minh, 2004). Air is introduced through the center of the cathode tube and oxygen ions diffuse through the solid oxide electrolyte to react with carbon in the liquid anode. As CO/CO_2 forms, bubbles develop which ascend to the surface when their buoyancy force exceeds the pressure exerted on them by the liquid anode.

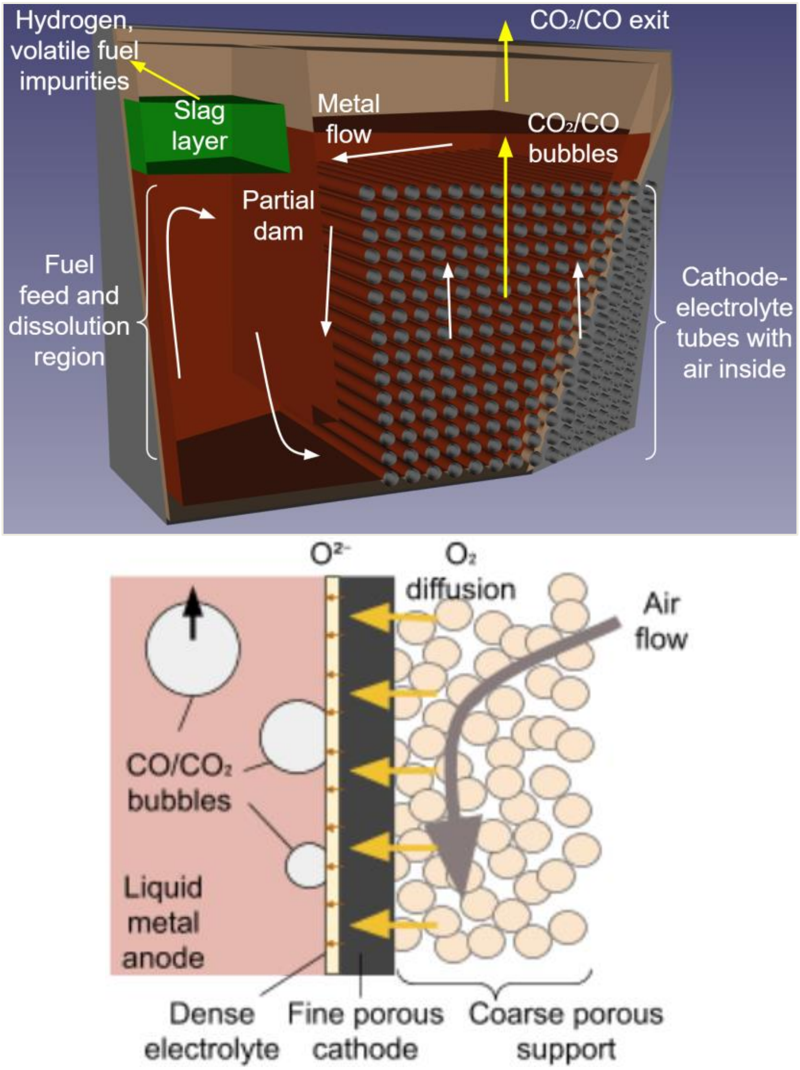

Figure 15: Top: Schematic of overall DCFC unit proposed by Boyd Davis, Adam Powell, and Uday Pal. Bottom: Section detail of the cathode, electrolyte, and anode interfaces.

Another embodiment of the proposed DCFC uses a porous ceramic block cathode with cut vertical passages coated in solid oxide electrolyte. Air could flow through the porous block, diffuse through the electrolyte surface, and react with carbon in the liquid anode filling the vertical passages. Geometry of this block could be optimized to promote electrochemical reaction sites and stirring of the liquid anode. This architecture could have a lower manufacturing cost relative to the tubular cathode/electrolyte geometry described earlier.

Overall, this cell design builds on knowledge of DCFC design from previous works by taking an approach that combines key innovations to ensure the highest likelihood of success. To achieve its desired functionality, developments in key components are required, namely a low-cost cathode/electrolyte and a liquid metal anode with high carbon solubility and low liquidus temperature.

3.1.1 Cathode/Electrolyte Development

The preliminary design for this DCFC is planned to use the closed-end tubular cathode/electrolyte arrangement with an outside diameter of approximately 20mm to 25mm. These will consist of a 1-2mm thick current collector support tube with 30% to 40% porosity surrounded by a 30μm to 50μm thick cathode and finally a 30μm to 80μm thick solid oxide electrolyte. Materials of construction considered for the current collector are a silver, nickel, or steel alloy foam. Cathode materials include LSM, lanthanum iron oxide (LSF), lanthanum nickel oxide (LNO), or lanthanum strontium cobalt ferrite (LSCF). Candidate materials for the electrolyte are zirconia doped with yttria or scandia (YSZ or ScSZ), or a ceria-based electrolyte doped with samarium or gadolinia (SDC or GDC). Further investigation into the fabrication and performance of this cathode/electrolyte is outside the scope of this thesis.

3.1.2 Anode Alloy Development

The key requirements of this liquid metal anode are a low liquidus temperature and high carbon solubility. It is well known that Fe exhibits high carbon solubility. This characteristic coupled with the abundance and relatively low cost of Fe makes it a great candidate for the basis of this DCFC anode alloy design.

The eutectic composition of an alloy corresponds to the lowest temperature at which a mixture of substances completely melts or solidifies. Steel, an alloy of Fe and C, has a eutectic composition of 4.3 wt.% C around 1150°C as shown at point (C) in **figure 16**. Using the Fe-C eutectic composition in a DCFC would require an operating temperature around 1200°C which is far too high for desirable electrochemical reactions and overall cell efficiency. Therefore, additional alloying elements were investigated to incorporate into the Fe-C system to lower liquidus temperature.

Sn has a melting point of 232°C and has shown been investigated for use with solid oxide electrolytes by Jayakumar, Pati, and Lagrille as discussed in section 2.2.3.3. However, Sn has low carbon solubility which negatively impacts one of the key requirements of this alloy. Fe-Sn-C data is nearly absent from literature and thermodynamic databases as Sn in steel segregates to grain boundaries which has a detrimental effect on mechanical properties (Watanabe et al., 1980). Examination of the Fe-Sn phase diagram in **figure 17** shows the eutectic composition at approximately 30 wt.% Sn.

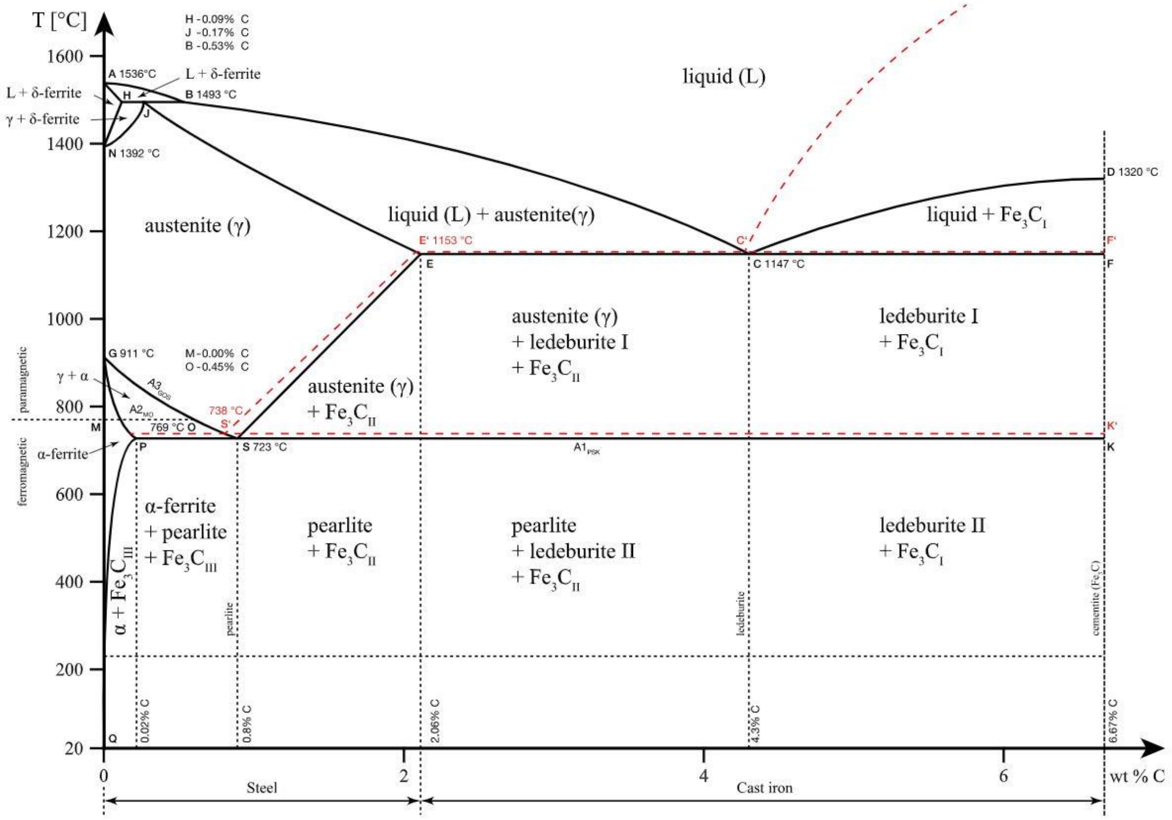

Figure 16: Fe-C Phase diagram (Velling, 2020). Dashed lines show differences in tie line locations upon heating vs. cooling with solid lines. This diagram is used as the starting point for DCFC liquid metal anode design.

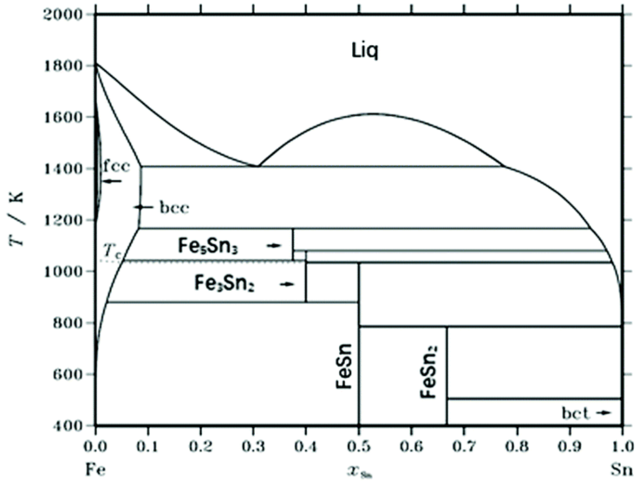

Figure 17: Fe-Sn Phase diagram (Lin et al., 2020).

In 2003 Gómez-Acebo et al. investigated low melting point alloys in the Fe-Cr-Mn-Mo-C system using Thermo-Calc software for the calculation of phase diagrams (CALPHAD) based on thermodynamic data. By projecting liquidus lines onto temperature-composition planes, they found a eutectic composition of Fe – 3.99 C – 21.4 Mn – 10.4 Mo with a liquidus temperature of 1036°C. This composition allows a decrease in liquidus temperature of over 100°C from the Fe-C eutectic while maintaining 93% of the carbon solubility, making Mn and Mo alloying elements of great interest to this DCFC anode alloy.

Si is commonly alloyed with steel to increase strength and improve magnetic properties (Lindeburg, 2020). It an important alloying element in cast iron as over approximately 1 wt. % Si forces carbon out of the solution creating the characteristic graphitic microstructure present in grey cast iron (Gillespie, 1988). Hoel found that adding Si to the Fe-Mn-C system, shown in **figure 18**, resulted in a liquidus temperature of 1000°C but reduced C solubility to 0.73 wt.%. Due to the presence of Si in nearly all steels, it is anticipated that some percentage of Si will be present in the anode alloy.

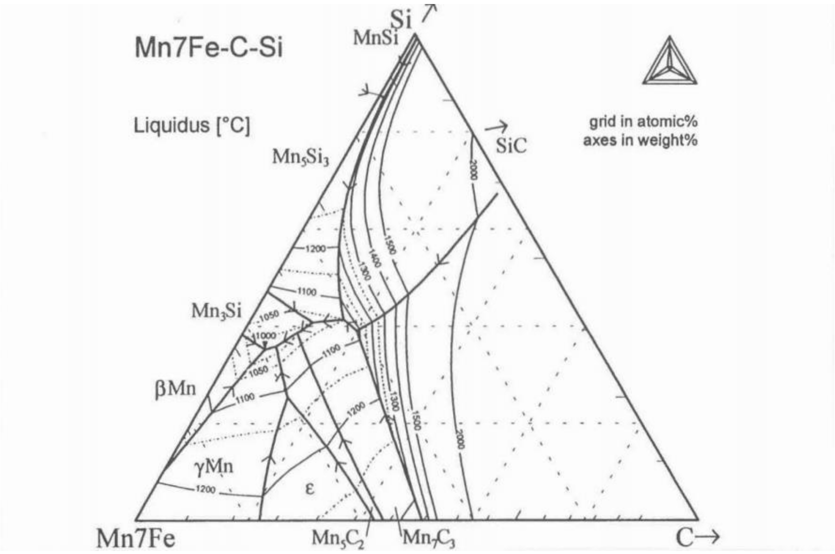

Figure 18: Mn7Fe-C-Si Ternary system liquidus surface (Hoel, 1995).

Ni is often alloyed with Fe to increase toughness, hardness, and corrosion resistance (Lindeburg, 2020). Ni is about half the cost of Mo, \$0.014/g vs. \$0.027/g (USGS, 2021), and as such is an attractive alternative alloying element for this liquid anode. Literature regarding liquidus temperatures of the Fe-Mn-Ni-C system could not be located, so Thermo-Calc software was used to assess the suitability of this system for a DCFC liquid anode.

3.1.2.1 Thermo-Calc Computational Model

Thermo-Calc software uses CALPHAD methodology to predict the interactions and properties of multi-component systems (Thermo-Calc, 2021). This method allows databases to be developed from a four-step process: Data capture, assessment, optimization, and storage shown in figure 19. Phases and reactions of the system are identified during the data capture step, while in the assessment step a Gibbs energy model is defined for each phase using coefficients fitted to thermodynamic data during optimization. The solubility model starts by equating the chemical potential of a solute in its crystal phase and in solution.

$$\mu_{solution}^{solute}(p,T) = \mu_{solid}^{solute}(p,T) \qquad [13]$$

Change in free energy associated with introducing an extra solute particle into the solution (Li, 2017) is:

$$\mu_{solution} = G_1 - G_0 \qquad [14]$$

$$where: G_a = -kTln(\Delta_a)$$

$$and\ \Delta_a = isobaric - isothermal\ partition\ f(N, p, T)$$

Where k is the Boltzmann constant [1.38x10^{-23} J/K], N is the number of particles of species a, while p and T are pressure and temperature.

Free energy of the mixed liquid is a function of the composition and free energy of species *i* in its pure liquid phase (Thermo-Calc, 2021). Gibbs energy per mole of solution phase is the sum of reference, configurational, and excess contributions.

$$G_m = G_m^0 + \Delta G_m^{ideal} + \Delta G_m^{excess} \qquad [15]$$

$$G_m^0 = \sum_{i=1} x_i G_i \qquad [16]$$

$$\Delta G_m^{ideal} = RT\big(x_i\ ln(x_i)\big) \qquad [17]$$

The excess contribution is determined by a Redlich-Kister polynomial fitting the changes in chemical potential of a species to phase transitions. For a binary system containing species A and B, excess contribution is:

$$G_m^{excess} = x_A x_B \sum_{k=0}^{k} L_{A,B}(x_A - x_B)^k \qquad [18]$$

Where L$_{A,B}$ is a coefficient used to fit a curve to the excess energies which can be determined via the method of least squares.

In the liquid phase, all elements of the system mix in one sublattice and G$_m$ is used to create a thermodynamic description of the multi-component mixture. The software then uses the free energy curves of each phase at every temperature interval to create a phase diagram, showing phases present at each composition and temperature for a particular pressure. An illustration showing how compositions are determined from Gibbs free energy is shown in **figure 20**.

Figure 19: CALPHAD Methodology followed by Thermo-Calc when developing thermodynamic databases (Thermo-Calc, 2021).

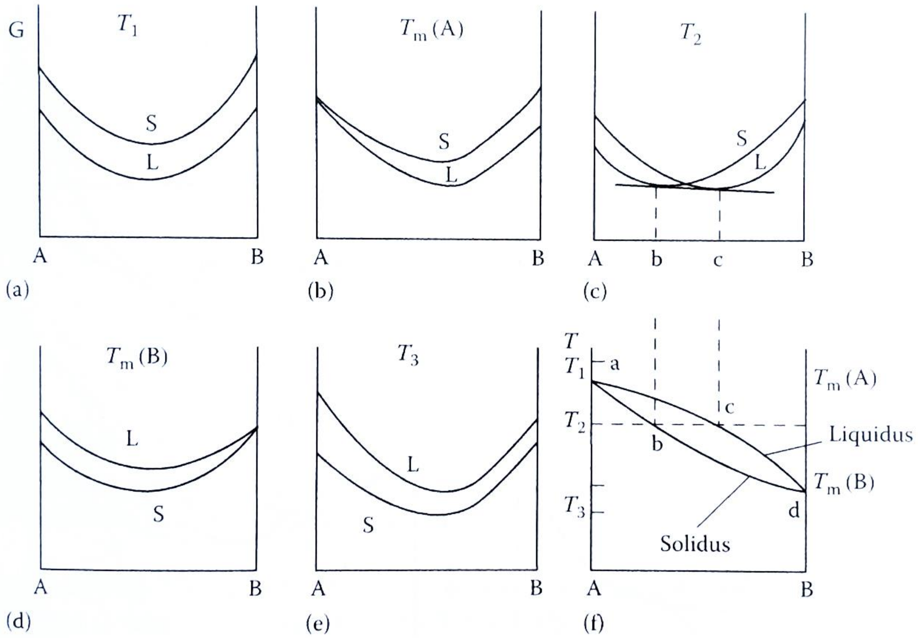

Figure 20: Derivation of a phase diagram (f) from the free energy curves of liquid and solid phases at various temperatures (Porter et al., 2009).

3.1.2.2 Using Thermo-Calc to investigate Anode Alloys

The investigation began by varying Mn and Ni content by increments of 5 wt. % to understand the influence of varying the composition of these elements on the overall liquidus temperature. An initial run of 30 compositions using the TCFE9 Thermo-Calc database resulted in the composition 56.1 Fe – 25 Mn – 15 Ni – 3.9 C that showed a liquidus temperature of 1055°C. A plot showing liquidus temperatures vs. carbon solubility of these 30 compositions can be examined in **figure 21**, corresponding to compositions listed in **Table 1**. This revealed using over 20 wt. % Mn and Ni in the system had advantageous results in reducing the liquidus temperature while retaining high (over 80% of that present in the Fe-C eutectic) carbon solubility. Further investigation using 30 wt. % and 40 wt. % Mn with varying levels of Ni and Fe showed lower liquidus temperatures illustrated in **figures 22** and **23** respectively. Compositions using 40 wt. % Mn with over 26 wt. % Ni experienced a sharp decrease in carbon solubility which is undesirable for the DCFC anode. For this reason, it was decided that the best compromise of low liquidus temperature with high carbon solubility occurred at a composition of 40 Mn – 30.5 Fe – 26 Ni – 3.5 C which has a liquidus temperature of 982°C shown in **figure 24**.

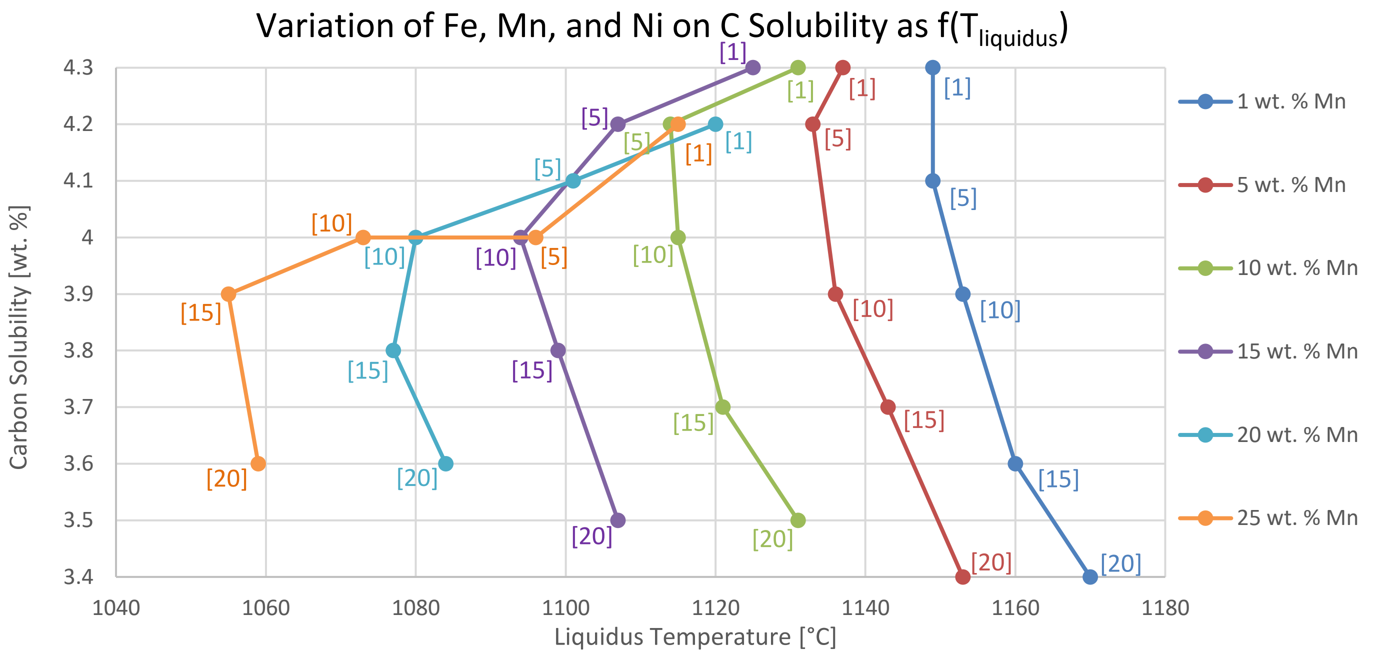

Figure 21: Comparison of liquidus temperature on carbon solubility in Fe-Mn-Ni-C system. Values in brackets correspond to Ni wt. % in the alloy. Compositions using higher (20 – 25 wt. %) Mn showed the lowest liquidus temperatures using between 10 and 20 wt. % Ni. These regions are investigated in **Figure 22** and **23** to realize further reductions in overall liquidus temperature.

Table 1: Initial assessment of Fe-Mn-Ni-C system.

Plot Number	Element [%wt.]				$T_{liquidus}$ [°C]
	Fe	Mn	Ni	C	
1	93.7	1	1	4.3	1149
2	89.9	1	5	4.1	1149
3	85.1	1	10	3.9	1153
4	80.4	1	15	3.6	1160
5	75.6	1	20	3.4	1170
6	89.7	5	1	4.3	1137
7	85.8	5	5	4.2	1133
8	81.1	5	10	3.9	1136
9	76.3	5	15	3.7	1143
10	71.6	5	20	3.4	1153
11	84.7	10	1	4.3	1131
12	80.8	10	5	4.2	1114
13	76	10	10	4	1115
14	71.3	10	15	3.7	1121
15	66.5	10	20	3.5	1131
16	79.7	15	1	4.3	1125
17	75.8	15	5	4.2	1107
18	71	15	10	4	1094
19	66.2	15	15	3.8	1099
20	61.5	15	20	3.5	1107
21	74.8	20	1	4.2	1120
22	70.9	20	5	4.1	1101
23	66	20	10	4	1080
24	61.2	20	15	3.8	1077
25	56.4	20	20	3.6	1084
26	69.8	25	1	4.2	1115
27	66	25	5	4	1096
28	61	25	10	4	1073
29	56.1	25	15	3.9	1055
30	51.4	25	20	3.6	1059

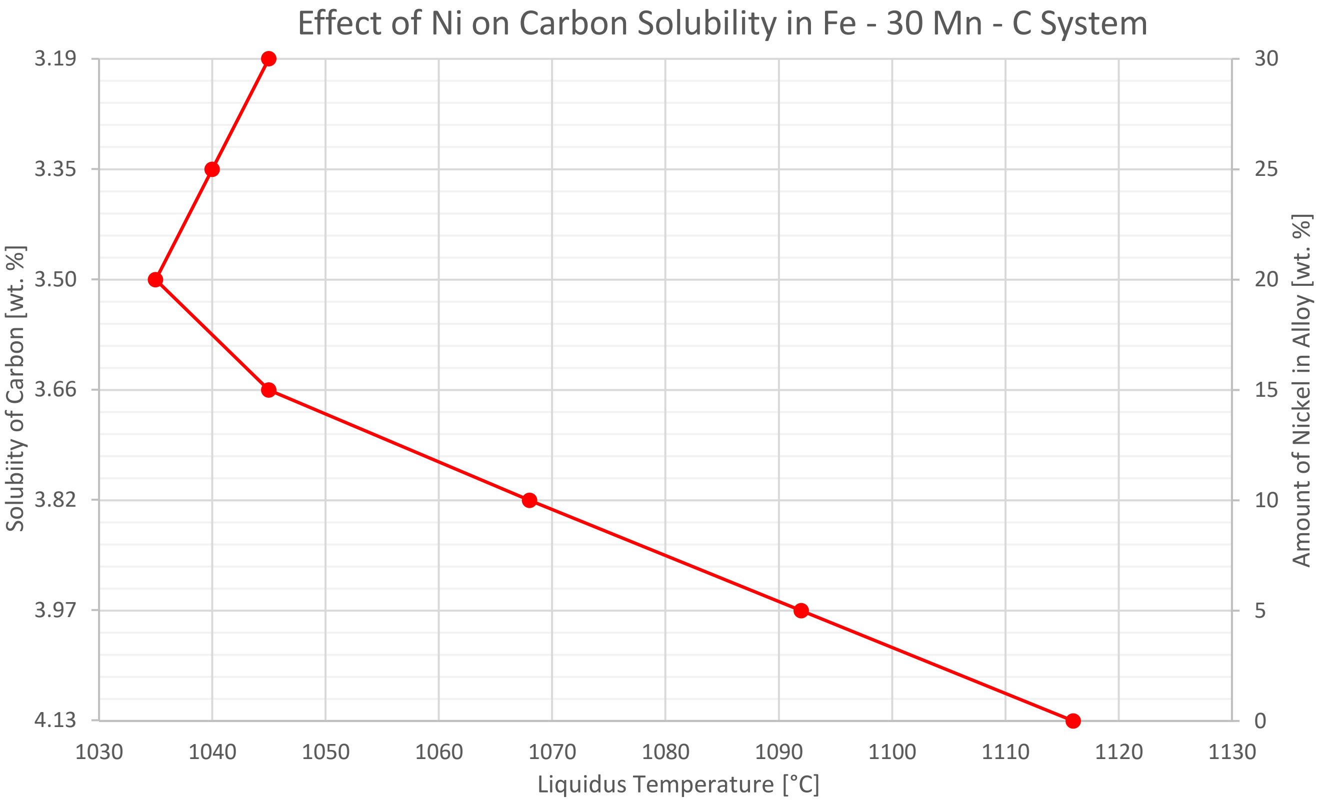

Figure 22: Effect of Ni addition to Fe – 30 Mn – C system.

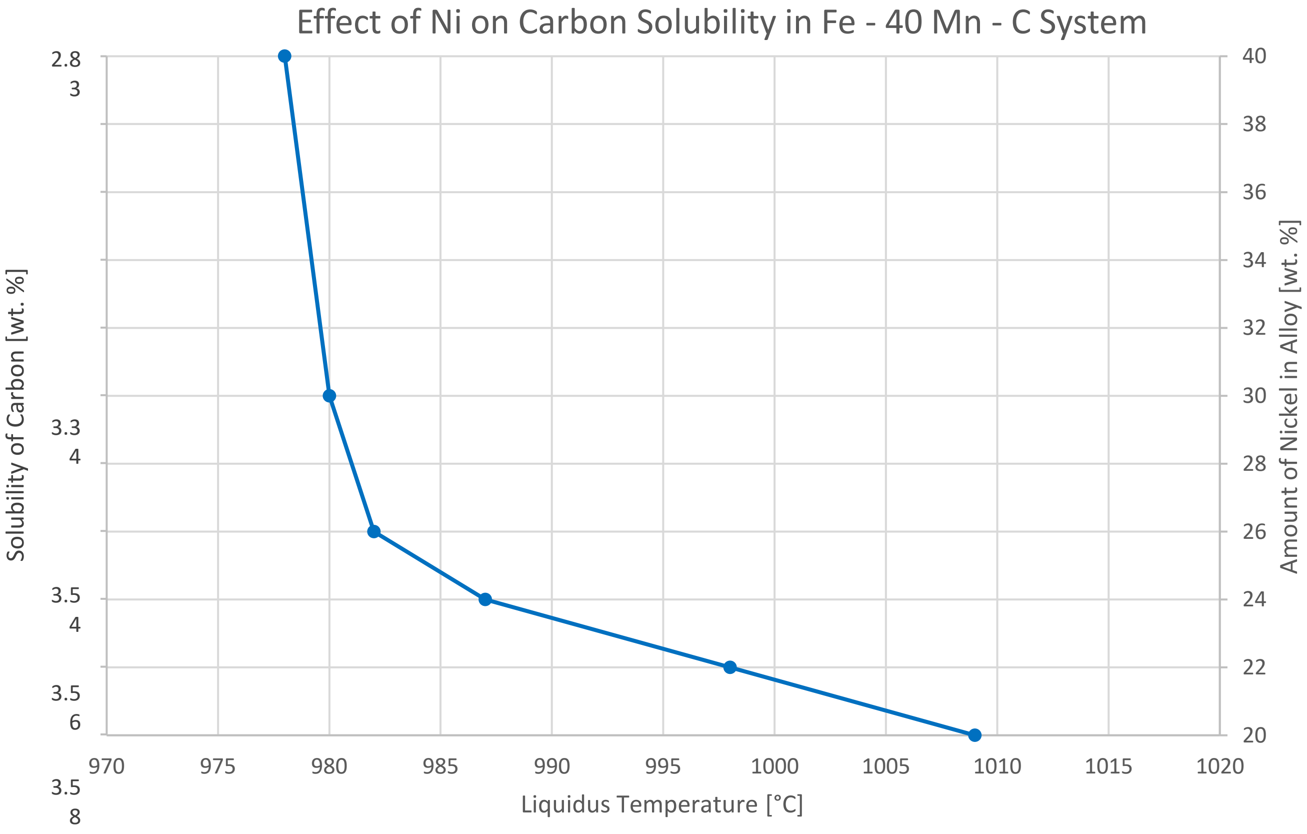

Figure 23: Effect of Ni addition to Fe – 40 Mn – C system.

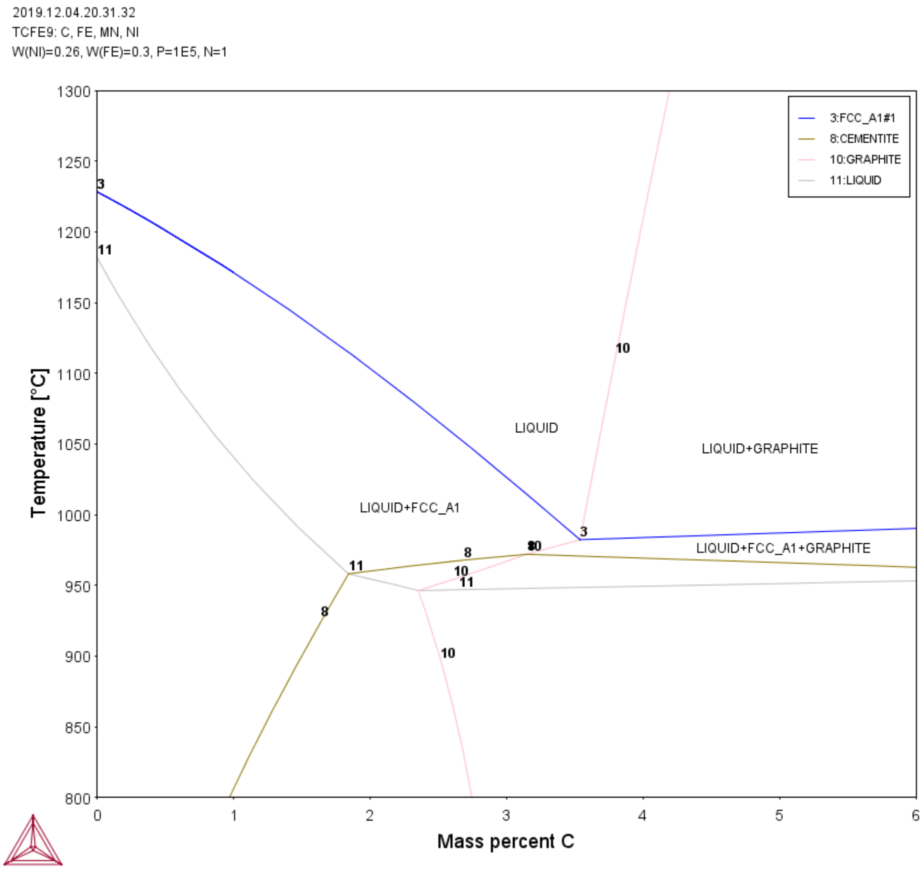

Figure 24: 40 Mn – 30.5 Fe – 26 Ni – C Phase diagram showing eutectic point at 3.5 wt. % C with a liquidus temperature of 982°C.

From this investigation it was determined the best candidates to alloy with Fe and C in the anode were: Mn, Mo, Ni, and Sn. To perform a more exhaustive analysis of potential compositions for this application, high-throughput calculations of the Fe – Mn – Ni – Si – C system were performed by the Integrated Materials and Processes Design (IMPD) group at WPI. Sn was not present in the thermodynamic database and was therefore omitted in this analysis. Using step size of 2.5 mol. %, 6280 combinations of alloys were tested from 0- 20 mol. % of Mn, Ni, Si, and C. The best candidate alloy found during this step, 52.3 Fe – 22.6 Mn – 20.9 Ni – 4.2 C had a liquidus temperature of 1050°C. The carbon solubility as a function of liquidus temperature from these combinations is visualized in **figure 25**. A second round of high throughput calculations were performed using with a step size of 0.5 mol % to find similar compositions with lower liquidus temperatures. 5441 additional compositions were generated, with the optimal composition containing 51.7 Fe – 20.3 Mn – 24 Ni – 4 C showing a liquidus temperature of 1031°C.

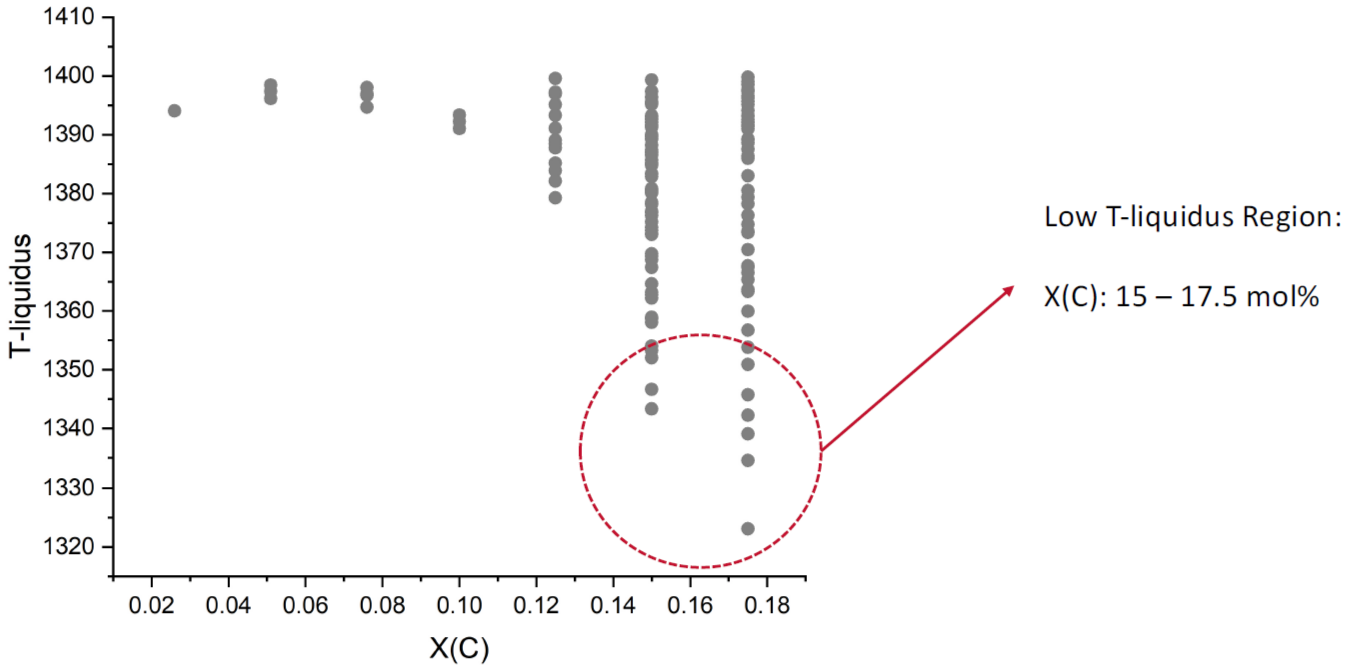

Figure 25: Results from first round (2.5 mol. % increments) of high throughput calculations performed by the IMPD group at WPI for the Fe-Mn-Ni-C system with Mn, Ni, and C below 20 mol %. The y-axis is in Kelvin and x-axis is in units of mol. %.

3.1.3 Anode Alloy Creation

With the knowledge gathered from this research, four candidate anode alloys were chosen for testing in an experimental high-temperature apparatus mimicking the proposed DCFC design. Listed in **Table 2**, these alloys were selected from directly from literature (alloy 1 and 4), selected considering previous works in conjunction with literature (alloy 2), or determined using CALPHAD methodology (alloy 3).

Table 2: Selected anode alloys for testing in DCFC.

Alloy No.	**Alloy System**	**Calculated Composition [wt. %]**							**Calculated Liquidus [°C]**	**Source**
		Fe	**Mn**	**Mo**	**Ni**	**Sn**	**Si**	**C**		
1	Fe-Mn-Mo-C	66	10	20				4	1036	Gómez-Acebo et al., 2003
2	Fe-Mn-Sn-C	37.5	30			30		2.5		Based on Fe-Sn phase diagram
3	Fe-Mn-Ni-C	30	40.5		26			3.5	982	CALPHAD
4	Fe-Mn-Si-C	12.9	76				10	1.1	1000	Hoel, 1995

Approximately 900g of each alloy was measured and placed in an alumina crucible, then melted using a Sentro-Tech ST-1600C-445 resistance box furnace at a temperature of 1500°C for 1.5 hours under atmospheric conditions.

3.1.4 Anode Alloy Validation

To verify liquidus temperature, differential scanning calorimetry (DSC) was performed on approximately 50 mg of each alloy by the Materials Laboratory for Energy and Environmental Sustainability at Boston University (BU). Temperature measurements from these tests showed little deviation from calculated values. To verify carbon content, LECO combustion analysis was performed by Applied Technical Services (ATS) on alloys 1-3. Additionally, electron dispersive spectroscopy (EDS) was performed on each alloy in a JSM 7000F scanning electron microscope (SEM) using three different locations 4mm apart on a sample weighing approximately 5g. SEM images of each alloy at x5000 magnification are shown in **figure 26**. The results from these measurements can be found in **table 3**. It is assumed that the alloys had a homogeneous distribution of elements throughout their bulk.

Table 3: Measured alloy compositions and liquidus temperatures before experiments.

Alloy No.	Alloy System	Data Point	Measured Composition [wt. %] via EDS								Measured C [wt. %] via LECO	Liquidus Temperature via DSC	
			Fe	Mn	Mo	Ni	Sn	Si	C	Sb		Heating [°C]	Cooling [°C]
1	Fe-Mn-Mo-C	1	65.3	10.1	14.5			2.5	7.6		4.97	1085	1025
		2	52.1	8.7	28.6			1.8	8.7				
		3	69.8	9.4	12.1			1.9	6.7				
		Avg.	62.4	9.4	18.4			2.1	7.7				
2	Fe-Mn-Sn-C	1	41.7	31.4			20.7	1.1	5.1	0	2.31	1090	1065
		2	31.3	33.7			29.1	0.2	5.7	0			
		3	39.4	31.8			21.7	1.3	4.9	0.9			
		Avg.	37.5	32.3			23.8	0.9	5.2	0.3			
3	Fe-Mn-Ni-C	1	34.1	37.8		21.4		0.5	6.2		4.29	1075	1000
		2	42.8	28		25.2		1	2.9				
		3	41.1	27.6		27.6		0.9	2.9				
		Avg.	39.3	31.1		24.7		0.8	4.0				
4	Fe-Mn-Si-C	1	13.2	73.4				8.6	4.7			1145	1045
		2	14.8	71.2				8.3	5.7				
		3	12.8	73.6				8.3	5.3				
		Avg.	13.6	72.7				8.4	5.2				

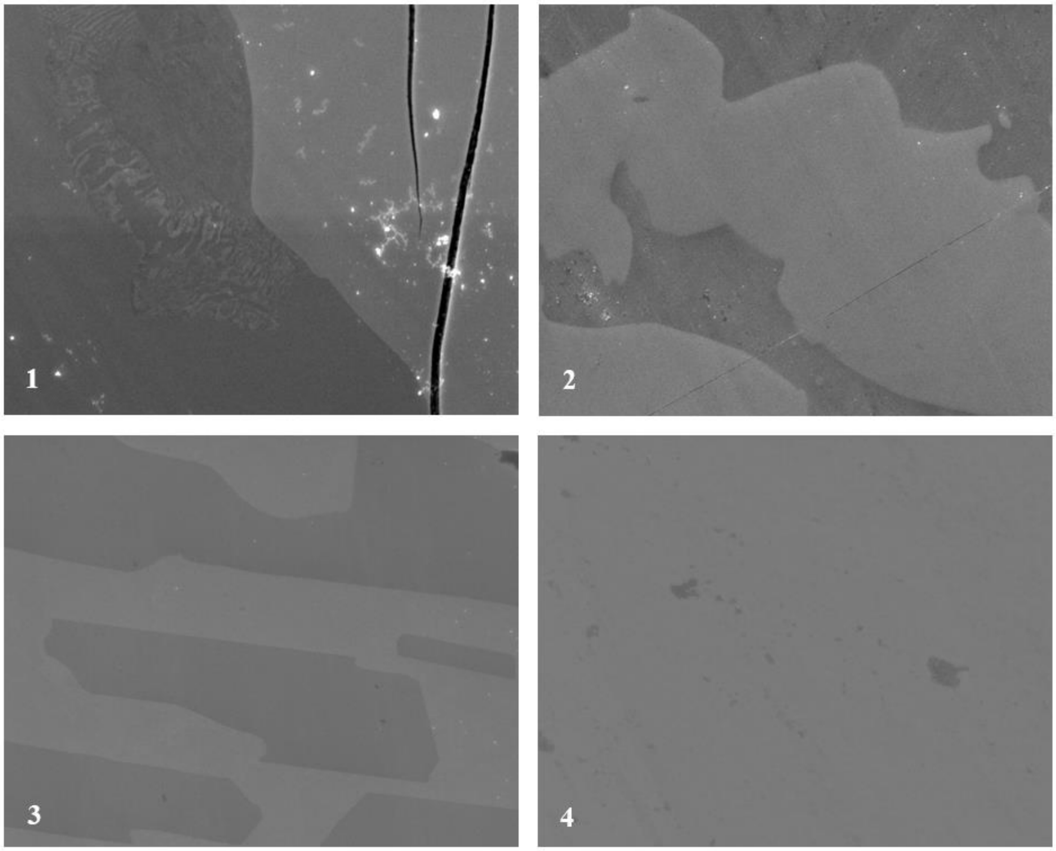

Figure 26: SEM images at x5000 magnification of each alloy as labeled.

3.2 Experimental Apparatus

A high-temperature controlled-atmosphere electrochemistry apparatus shown in **figure 27** was used to obtain OCV measurements using the candidate alloys listed in **table 2**. The apparatus was assembled from a 26” section of 6” NPS Sch 40 310 SS pipe with a 0.375” thick flanged connection at the top and a 0.25” thick cap welded at the bottom. The upper flange of the apparatus of three 1/4-20 threaded rods suspending a 0.075” thick 304 SS sheet approximately 5.75” in diameter. This sheet was approximately 4” from the bottom of the outer tube and used as a platform to place a 240 ml alumina crucible containing the anode alloy. Kurt Lesker vacuum coupling ports in the top flange allowed for mounting of two thermocouples, a 0.5” diameter graphite rod used as an electrode and source of carbon fuel for the reaction, a 0.75” OD YSZ electrolyte tube with a closed hemispherical end and wall thickness of 2mm, and two 0.125” fittings used for inert gas inlet and outlet connections. Distance between the electrolyte tube and graphite rod centerlines was approximately 2.25” and thermocouples were located at radii of 1.5” and 2.5”. Three heat shields were spaced 1.5” apart and mounted on the 1/4-20 threaded rods, with the uppermost shield approximately 6” from the top flange. Use of these shields reduced the temperature of the top flange to about 100°C at the maximum furnace temperature of 1170°C.

This apparatus was lowered into an 18” diameter Mellen resistance furnace, with only the flanges resting on a support frame constructed of Unistrut. Furnace temperature was increased 10°C/min up to 950°C then used a 2°C ramp rate between 950°C and 1170°C to reduce likelihood electrolyte failure due to thermal stresses. Before starting the experiment, argon (Ar) inert gas was used to purge the apparatus chamber so that oxygen partial pressure was below 0.5%. Approximately 20g of Ag shot was poured into the electrolyte tube to be used as a cathode current collector. A 0.25” OD SS tube was inserted into the electrolyte tube to allow oxygen from ambient air to be introduced to the electrolyte due to the difference in partial pressures between ambient conditions and the apparatus.

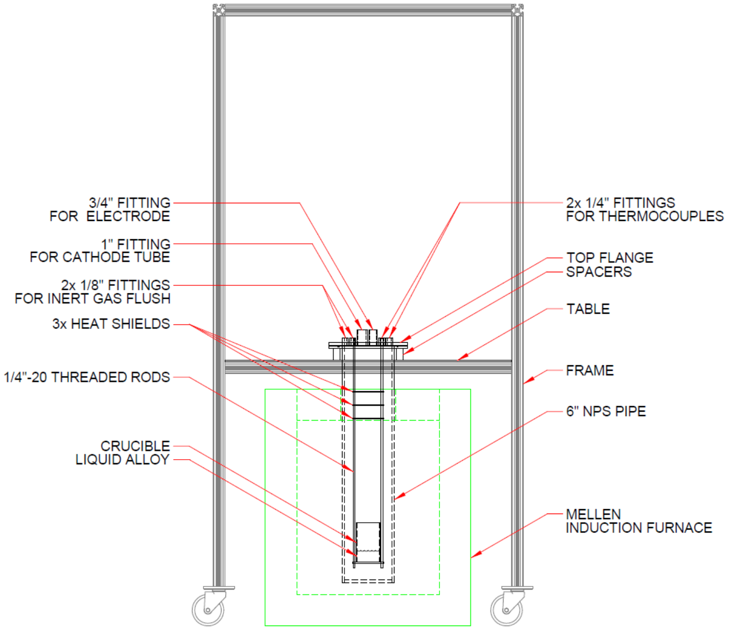

Figure 27: High temperature controlled-atmosphere electrochemistry apparatus.

4. Performance Models

4.1 Mass Balance

As mentioned in chapter 1, an attractive characteristic of DCFCs is their ability to operate on a variety of carbonaceous fuels. Considering the DCFC design proposed here, it is inevitable that impurities from the fuel will be present in the anode alloy as a slag layer or dissolved in the amorphous liquid phase. To better understand the amount of impurities that may accumulate in a commercial version of this cell, a 22-element mass balance was created for 13 different types of carbonaceous solid fuels. Fuel composition was obtained for fuels such as coal, to biomass, to off-specification building materials (Masiá et al., 2007) and charcoal (Elsayed et al., 2016). Compositions presented in those works are presented in **table 4**.

Table 4: Compositions of various solid carbonaceous fuels (Masiá et al., 2007).

Fuel	**Ash [wt. %]**	**Pure Elements [wt. % of total]**					
		C	**H**	**N**	**S**	**O**	**Cl**
Coal	12.5	70.08	4.79	1.51	0.59	10.52	0.01
Pine Chips	5.95	49.66	5.67	0.51	0.08	38.07	0.06
Corn Straw	7.65	44.73	5.87	0.6	0.07	40.44	0.64
Rape Straw	4.65	46.17	6.12	0.46	0.10	42.47	0.03
Biomass Mix	12.49	49.59	5.79	2.43	0.74	28.87	0.09
Pressure Ground Wood (PGW)	31.79	48.31	7.63	1.03	0	11.19	0.05
B-Wood	1.85	50.37	6.93	1.03	0	39.75	0.07
Palm Kernels	5.14	48.23	6.19	2.61	0.26	37.36	0.21
Olive Res.	7.17	54.12	5.36	1.28	0.21	31.66	0.20
Pepper Plant	14.44	36.11	4.26	2.72	0.49	41.86	0.13
Chicken Litter	37.79	37.38	4.19	3.76	0.74	15.64	0.50
Meat and Bonemeal (MBM)	23.95	43.07	6.04	9.16	1.27	15.64	0.87
Charcoal *(Elsayed et al., 2016)*	4.27	57.3	3.16	0	1.53	0	0.10

4.1.1 CO/CO_2 Formation Ratio as a Function of Temperature

The mass balance started by determining the amount of carbon available for the electrochemical reaction. On a per unit mass basis, fuel added to the system was multiplied by the wt. % carbon reported for the fuel type. With the amount of carbon present, amounts of CO and CO_2 that could be calculated. To do this accurately, one must consider the formation of CO and CO_2 as a function of temperature. Giddey et al. outlined the direct and indirect carbon oxidation reactions that could occur in a DCFC:

$$C + O^{2-} \rightarrow CO + 2e^{-} \quad [19]$$

$$CO + O^{2-} \rightarrow CO_2 + 2e^{-} \quad [20]$$

$$C + CO_2 \rightarrow 2CO \quad [21]$$

$$2CO + 2O^{2-} \rightarrow 2CO_2 + 4e^{-} \quad [22]$$

At atmospheric pressure the ratio of CO/CO_2 is equal around 690°C. Above this temperature, CO formation in [13] is favored, which is undesirable in a DCFC due to only two electrons exchanged per molecule of carbon fuel rather than four shown in [8]. Additionally, CO produced can react with carbon in the anode via the chemical (rather than electrochemical) reaction in [15], known as the reverse Boudouard reaction. This is detrimental to fuel cell performance since it uses carbon in the anode without contributing to cell voltage. The best way to avoid losses associated with CO formation is to operate the cell below the temperature at which equation [15] becomes energetically favorable about 700°C (Giddey et al. 2012). For an electrochemical cell operating above this temperature, CO_2 generated from equations [8], [13], [14], and [16] can be purged from the anode chamber to mitigate performance losses from equation [15]. Considered as a partially reacted fuel, CO that leaves the cell with CO_2 exhaust could be used in a downstream SOFC to improve system efficiency.

CO/CO_2 equilibrium ratio as a function of temperature was calculated based on Gibbs Free Energy (ΔG) of each reaction. **figure 28** shows the CO/CO_2 generation ratio as a function of temperature. The CO_2 reaction is desirable in the DCFC because of the four electrons exchanged per mole of carbon reactant versus two in the CO reaction. By increasing pressure, the temperature at which CO/CO_2 evolution is in equilibrium is elevated almost 100°C shown in **figure 29.**

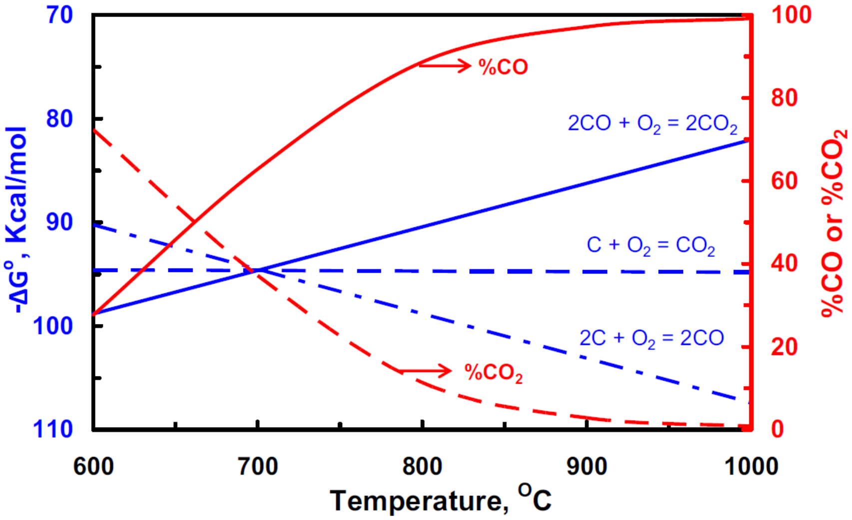

Figure 28: Ratio of CO/CO_2 produced between 600°C to 1000°C at atmospheric pressure (Giddey et al. 2012).

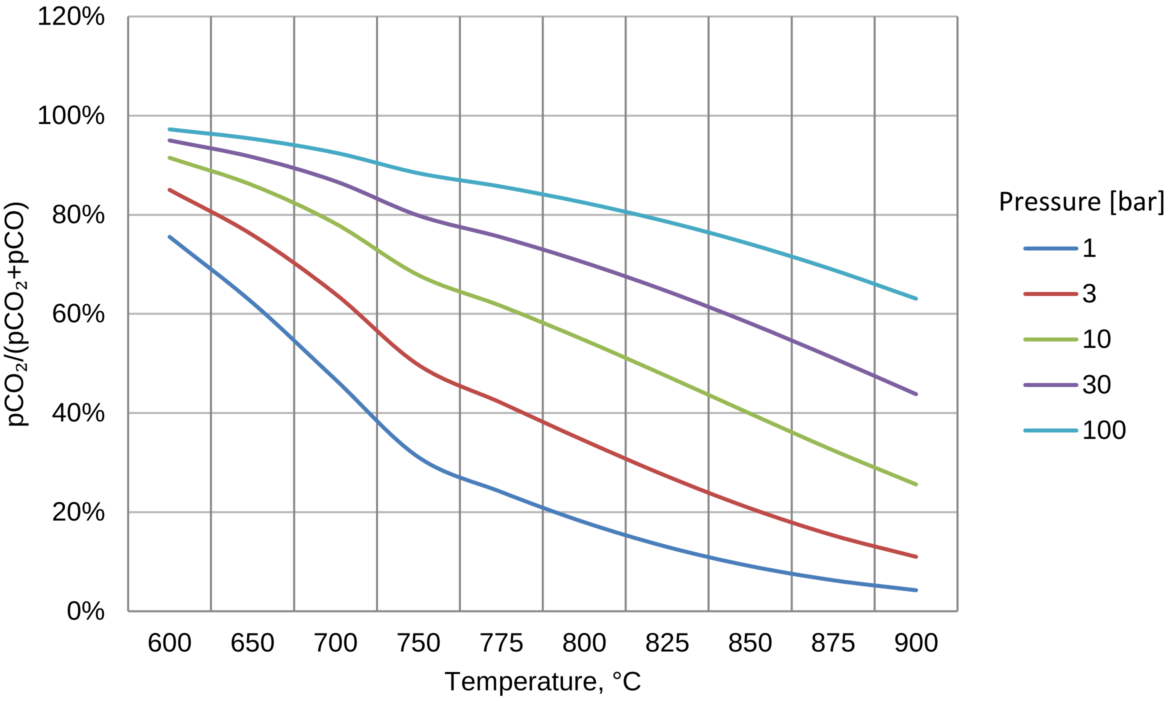

Figure 29: CO_2 gas fraction in equilibrium with carbon and CO at various pressures.

4.1.2 Pressure at the Reaction Site

Knowing the composition of candidate alloys from **table 2**, density of the liquid anode can be determined. To calculate the pressure at the electrolyte-anode interface at a vertical distance h below the liquid anode surface, the following equation was used:

$$P = P_0 + \rho_{alloy} g h \qquad [23]$$

Using alloy 3 ($\rho = 7.8$ g/cm^3) in an anode chamber with a depth of 1m results in a pressure difference of 77 kPa between the liquid surface and the bottom of the container. To achieve a pressure of 10 bar at the submerged electrolyte/anode interface via hydrostatic pressure alone would require an anode pool with a depth of 11.9m. Therefore, increasing the alloy volume to achieve a pressure of 10 bar to promote CO/CO_2 equilibrium at higher temperatures is not feasible due to physical and economic constraints. To achieve this desired pressure at the reaction site 1m below the liquid surface, pressure at the liquid surface would need to be 9.25 bar. A real-world DCFC unit would use the least amount of alloy possible, resulting in a higher pressure at the liquid surface. The geometry and construction of a DCFC designed to handle this pressure is outside the scope of this thesis.

4.1.3 Calculating Products from Reactions within the DCFC

With the CO/CO$_2$ equilibrium data, mass of each product evolved at a specific DCFC operating temperature considering the mass of carbon available, C_m, in a specific fuel type.

$$C_m = m_{fuel\ introduced} * wt.\%_{C\ in\ fuel} \tag{24}$$

$$CO = \frac{\%CO_{evolved} C_m}{M_C / M_{CO}} \tag{25}$$

$$CO_2 = \frac{\%CO_{2\ evolved} C_m}{M_C / M_{CO_2}} \tag{26}$$

Where M_i is the molar mass of species i. Total mass of oxygen required for the system was calculated via:

$$O_{m,\ total} = \Sigma O_{Req.\ for\ oxides} - O_m \tag{27}$$

Where O_m is mass of oxygen in the fuel. Total air required for the reactions was calculated by dividing $O_{m,\ total}$ by the wt. % of oxygen gas in air at 1 atm and multiplying by a factor (e.g. 50%) to account for only a fraction of the oxygen introduced actually taking part in the formation of oxides. Remaining oxygen would exit the cathode tube in a nitrogen-rich gas stream.

Effects of impurities in the fuels accumulating within the liquid anode alloy include an increase in liquidus temperature and a reduction in carbon solubility, both of which are detrimental to overall DCFC performance. Operating temperature of the unit will not be high enough to reduce oxides in the fuel to their alloys, so all of ash content in the fuel is considered to contribute to slag formation in the feed section. The mass balance model took a conservative approach and approximated that 20% of Si present in the fuel would be dissolved in the alloy, which reduces carbon solubility (Hoel, 1995).

$$wt.\%_{Si\ in\ fuel\ dissolved\ in\ alloy} = 1 - \left(wt.\%_{Si\ in\ fuel} * \%\ Si\ to\ slag\right) \tag{28}$$

$$wt.\%_{Si\ in\ alloy} = wt.\%_{Si\ in\ fuel\ dissolved\ in\ alloy} \left(\frac{m_{fuel\ added}}{m_{alloy,total}}\right) \tag{29}$$

$$m_{alloy\ removed} = wt.\%_{contaminated} m_{alloy,total} \tag{30}$$

$$where: wt.\%_{contaminated} = wt.\%_{Si\ in\ alloy}$$

Make-up elements required were determined by the composition of the anode alloy and amount removed. Carbon from the incoming fuel is used to replenish the mass of carbon removed with the contaminated alloy, with [24] becoming:

$$C_m = \left(m_{fuel\ introduced} * wt.\%_{C\ in\ fuel}\right) - \left(m_{alloy\ removed} * wt.\%_{C\ in\ alloy}\right) \tag{31}$$

It should be noted that the slag layer present in the feed section may attract all impurities from the fuel, keeping the anode alloy composition relatively consistent. In this case the inlet and outlet streams of make-up and contaminated alloy could be removed from the model.

The resulting flow diagram for a commercial DCFC is shown in **figure 30**. The values shown are for steady state operation; in reality the anode alloy and slag could be removed periodically with fuel and make-up elements introduced via loss-in-weight feeders at a corresponding interval to keep the mass of the system in equilibrium.

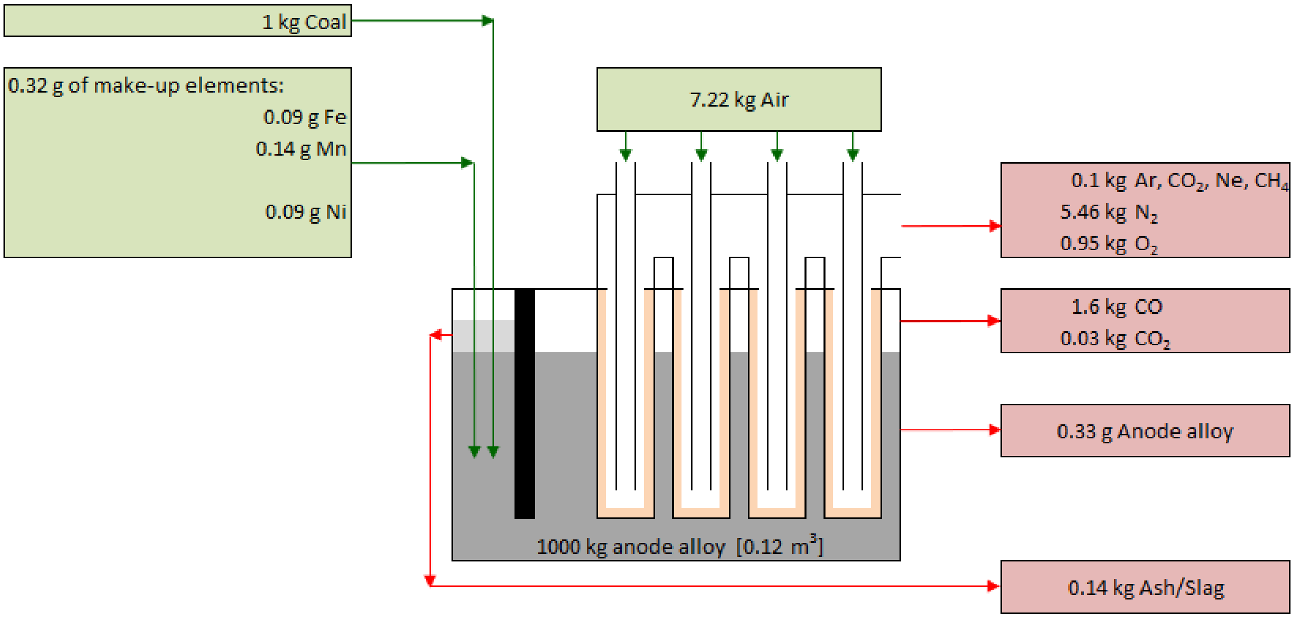

Figure 30: Flow diagram of proposed DCFC with tubular cathode/electrolyte architecture for mass balance in steady-state operation at 1000°C using an anode alloy comprised of 30 Fe – 40.5 Mn – 26 Ni – 3.5 C. Oxygen present in the exhaust gas stream corresponds to a 50% utilization factor (i.e. twice the required oxygen was introduced). Note total mass of make-up elements does not equal mass of anode alloy removed. The 0.01 g difference is replenished from part of the carbon delivered by the incoming coal fuel, with the remainder being used for CO/CO$_2$ production.

With the mass balance complete, fuel types can be ranked based on their suitability for the device. The most economical carbonaceous fuel is one that offers the highest carbon content with the smallest amount of impurities. Higher carbon content allows for more reactant to enter the cell and reduces storage volume and transfer cost per unit mass of fuel. Impurities in the fuel contribute to slag buildup in the feed chamber and contaminated anode alloy, both of which should be reduced as much as possible. **Figure 31** shows an analysis of the carbon content, ash/slag produced, and make-up alloy required using each fuel type with the 40 Mn – 30.5 Fe – 26 Ni – 3.5 C alloy. From this it can be discerned that B-grade wood, palm kernels, and olive residue are the best fuel choices for this alloy, providing the best ratio of carbon content to impurities per unit mass.

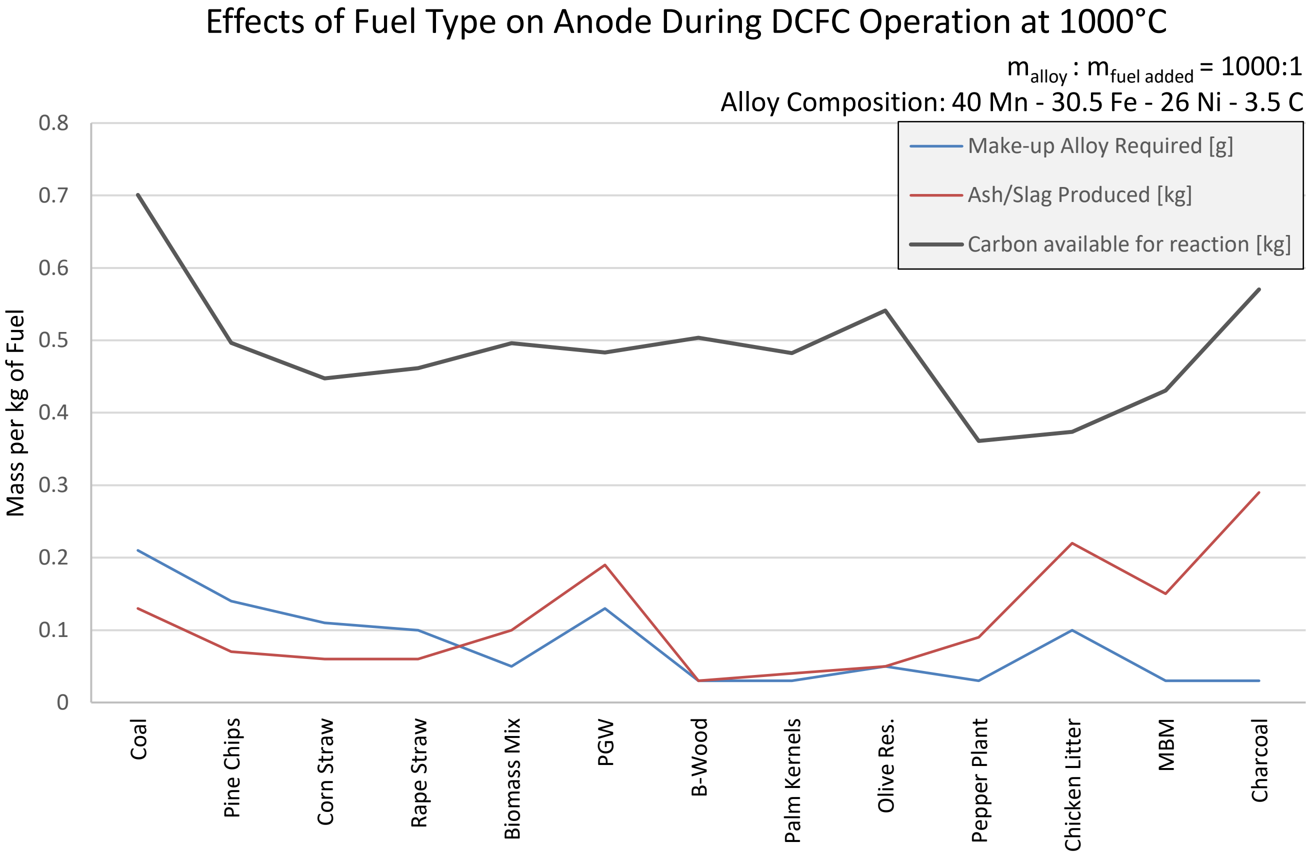

Figure 31: Analysis of carbonaceous fuel types for suitability with the 40 Mn – 30.5 Fe – 26 Ni – 3.5 C liquid anode alloy. Note alloy make-up mass is in g, not kg.

4.2 Energy Balance

To forecast the performance of this design, an energy balance was performed. First, enthalpy (H) and entropy (S) for each species was determined via the Shomate Equation with constants obtained from the National Institute of Standards and Technology (NIST) Chemistry WebBook, SRD 69. This data used to calculate available free energy (G) of a species from 25°C to 1300°C at a specified pressure via the following equation:

$$G(p,T) = H - TS \quad [32]$$

With this data obtained for C, O, CO, and CO_2, change in Gibbs free energy (ΔG) was calculated using [29], [29a], and [29b] for each of the following reactions below:

$$C + O_2 \rightarrow CO_2 \quad [33]$$

$$C + \left(\frac{1}{2}\right) O_2 \rightarrow CO \quad [34]$$

$$\Delta G = \Delta H - T\Delta S \quad [35]$$

$$\Delta H = mol._{prod.} H_{prod.} - (\Sigma mol._i \, H_i) \quad [35a]$$

$$\Delta S = mol._{prod.} S_{prod.} - (\Sigma mol._i \, S_i) \quad [35b]$$

Theoretical voltage of each reaction was calculated across the temperature range using the Nernst equation, which correlates the reduction potential of an electrochemical reaction to electromotive force, E, with units of volts. E is related to ΔG under standard conditions by:

$$\Delta G^0 = -nFE^0 \quad [36]$$

Where n is the number of electrons transferred in the reaction (2 for CO and 4 for CO_2) and F is the Faraday constant, equal to ~ 96485 C/mol. Given that the DCFC will experience non-standard conditions due to increased pressure and temperature to improve performance, these conditions must be accounted for in the calculation of ΔG for the DCFC energy balance.

$$\Delta G = \Delta G^0 + RTln(Q) \quad [37]$$

Substituting expression from [36] for ΔG in [37] and solving for E results in:

$$E_{th} = E^0 - \frac{RT}{nF} ln(Q) \quad [38]$$

With Q being the reaction quotient, a value that relates quantities of products and reactants in the overall reaction. Here Q was calculated using the partial pressure of oxygen gas from the incoming air and partial pressure of CO or CO_2 produced as a function of DCFC operating temperature per the reverse Boudouard reaction.

$$Q_{Product} = \frac{pO_2}{pProduct(T)} \quad [39]$$

Due to the wide range of temperatures that promote both CO and CO_2 production, total theoretical cell voltage was calculated by multiplying the theoretical voltage of each product by its fraction evolved, shown in [40].

$$E_{th,total} = \left(E_{th,CO} * \%CO\ evolved\right) + \left(E_{th,CO_2} * \%CO_2\ evolved\right) \quad [40]$$

Current density and power density were then determined using theoretical voltage values for the CO and CO_2 reactions and properties of the solid electrolyte. Conductivity and resistance values for three potential solid oxide electrolyte materials (YSZ, ScSZ, and SDC) were incorporated into the energy balance. Overall resistance of the electrolyte was calculated via dividing thickness by resistance per unit area:

$$r_{el.} = \frac{t_{electrolyte}}{k_{electrolyte}} \quad [41]$$

Current density is the quotient of E_{th} and $r_{el.}$ as shown below.

$$j = \frac{E_{th,total}}{r_{el.}} = \left[\frac{A}{cm^2}\right] \quad [42]$$

Power density, P_e, was calculated using $E_{th,\ total}$, j, and number of electrons transferred per mole of oxygen.

$$P_e = \frac{E_{th,total} j}{n} \quad [43]$$

4.2.1 Losses in an Electrochemical Reaction

Actual cell voltage is lower than the theoretical value due to losses present in the cell, including ohmic, concentration, and activation polarization (Kakaç et al., 2007).

$$V_{actual} = E_{th,total} - losses \quad [44]$$

Ohmic polarization accounts for the resistance encountered by electrons as they move through the fuel cell's electrodes. This can be expressed as:

$$\eta_{ohm.} = j(ASR_{ohm.}) \quad [45]$$

Where ASR_{ohm} is the area-specific resistance of the cell, and includes ionic resistance of the electrolyte, electronic resistance of the electrodes, and some contact resistance associated with the interfaces between cell components (Yoon et al., 2007).

Examining the electrolyte interfaces at a micro scale there exists a gradient in reactants on the anode and cathode sides. As reactants are combined and carried away (via buoyant force), the concentration of reactants at the electrolyte interface decreases. In a steady state condition, more reactants are continually transported from the bulk to the electrolyte reaction interface, moving from a region of high concentration in the bulk to the lower concentration at the interface. Concentration polarization accounts for this reduction in the concentration of reactants at the electrolyte surface as the reaction proceeds and was calculated using the equation below as presented by Kakaç et al.

$$\eta_{con.} = \frac{RT}{nF}\left(1 - \frac{1}{n}\right) \ln\left(\frac{j_L}{j_L - j}\right) \quad [46]$$

Where j_L is the limiting current density. This is defined as the minimum flux (the amount of a species flowing through an area, in this case the electrolyte surface) of carbon from the anode and oxygen ions from the cathode to the surface. For the anode, the limiting current density was calculated by:

$$j_{L,anode} = nFJ = nF\left(\frac{D_{C\ in\ maj.}\rho_{mol.,C}}{L}\right) \quad [47]$$

Where D is the diffusivity of C in the major constituent of the alloy and ρ is the molar density of C in the liquid alloy. The boundary layer thickness, L, was estimated to be 100μm in the liquid anode.

For the cathode, limiting current density was calculated using the Nernst-Plank equation with convective molar flux added (Perez, 2004).

$$j_{L,cathode} = nFJ\left(\frac{\partial c}{\partial x}\right)_{x=0} + Cv = nFD_{O_2\ in\ air}\left(\frac{c_0}{\delta_n}\right) + Cv \quad [48]$$

Where c^0 is the initial concentration of oxygen ions before any flow of current, and δ_n is the thickness of the diffusion boundary layer. Limiting current density in the cathode can be increased by decreasing the diffusion boundary layer (Filzwieser et al., 2002). The second term represents convective molar flux due to fluid motion, where C is the ionic concentration and v is hydrodynamic velocity of air travelling through the cathode tube, estimated to be 2 m/s.

Activation polarization accounts for the portion of energy required to overcome an activation barrier which allows the electron-exchanging reaction to occur. This energy comes from a portion of the reaction voltage generated, decreasing actual cell voltage. Yoon et al. defined the activation polarization as:

$$\eta_{act.} = \frac{2RT}{F}\ln\left[\frac{1}{2}\left(\left(\frac{i}{i_0}\right) + \sqrt{\left(\frac{i}{i_0}\right)^2 + 4}\right)\right] \quad [49]$$

Where i_0 is the exchange current density, a measure of the electrocatalytic activity at the triple phase boundary (the electrolyte-liquid anode interface where O^{2-} reacts with C to produce CO_2) and quantifies the rates of reactions at the anode and cathode (Yoon et al., 2007). Exchange current density can be determined by curve fitting empirical voltage data as a function of current density. Without such data, $\eta_{act.}$ was omitted from this energy balance.

4.2.2 Other Losses

Voltage calculated refers to that produced by the anode, cathode, and electrolyte arrangement in a single cell. To achieve a desired voltage, many cells can be connected by electrical leads. Using terminology taken from planar fuel cell arrangements, this setup is called a fuel cell stack. Thermal energy lost through the leads can be mitigated by using a material with low thermal conductivity, but the same material will also have low electrical conductivity since thermal and electrical conductivity are coupled through the Wiedmann-Franz law. The voltage drop per lead can be calculated from the minimum total energy lost due to resistance and thermal energy (Powell, 2010) shown below.

$$V_{el} = 2\sqrt{L_{el}T\Delta T} \quad [50]$$

$where: T = operating\ temperature$

$\Delta T = T - T_{ambient}$

Some heat from the DCFC will be required to raise the temperature of reactants as they enter the device. Heat [kJ/mol] required for incoming air and present in the cathode air exhaust was converted to volts via [36] in the expression below:

$$V_{gas,in} = \frac{\left(mol._{air,introduced} / mol._{O_2\ in\ air} \right) C_{p,air} \Delta T}{nF} \qquad [51]$$

$$V_{gas,out} = V_{gas,in} \left(mol._{air,exhaust} / mol._{O_2\ in\ exhaust} \right) \qquad [52]$$

This amount of heat lost by the cell can be reduced by using waste heat from the exhaust gas to heat incoming air. Industrial heat exchangers used in such applications are referred to as economizers and can reach heat transfer efficiencies, ε, up to 90% (Lindeburg, 2020). Using this factor, total heat lost due to the incoming ambient air stream is:

$$V_{air} = V_{gas,in} - (1 - \varepsilon)\, V_{gas,out} \qquad [53]$$

Energy required to heat incoming solid fuels could similarly be reduced by using the CO/CO_2 exhaust gas stream in a heat exchanger. This calculation was not included in the study.

During operation, heat radiated from the DCFC unit to the surrounding air will also contribute to thermal losses. These losses are considered negligible compared to the thermal and electrical losses calculated above and were omitted from this analysis.

Overall cell efficiency was calculated by subtracting thermal losses from the heat produced, ΔH, from the CO/CO_2 reaction at a specified operating temperature.

$$Efficiency = \frac{\Delta H_{total} - V_{el} - V_{air}}{nF} \qquad [54]$$

4.2.3 Modified DCFC Evans Diagram

A plot showing the relationship between electric potential and current density is called an Evans diagram. Such a plot is often adapted to show performance of a fuel cell by including power density values as a function of current density on a second vertical axis. Using this format, values obtained from the energy balance are presented for the proposed DCFC operating at 800°C in **figure 32**, with operation at 1000°C shown in **figure 33**. Overall performance is depends on many variables, with their values listed in the dashboard at the top of the plot. As current density varies from its minimum to maximum (the limiting value dictated by the anode, cathode, or electrolyte), actual cell voltage decreases to zero. Since power density is the product of voltage and current density, it exhibits a parabolic shape with its highest value corresponding to the ideal cell operating condition.

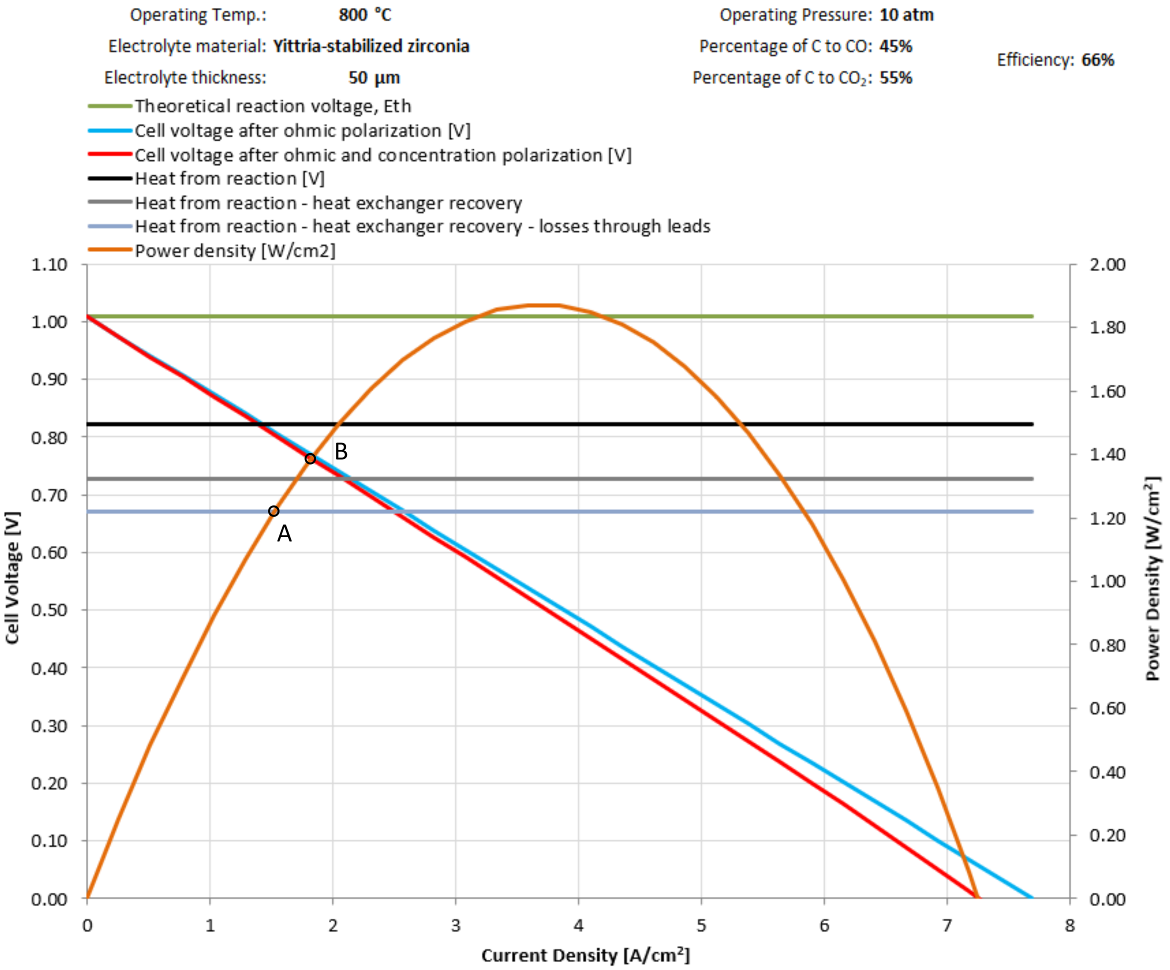

Figure 32: Modified DCFC Evans diagram with dashboard representing target values of operation. Peak calculated power density using a YSZ electrolyte in these conditions is 1.87 W/cm^2. However, the cell will have to be operated between points A and B due to thermal and electrical losses, resulting in a maximum power density of 1.37 W/cm^2. Under the same conditions using ScSZ electrolyte, a power density of 3.25 W/cm^2 is forecasted.

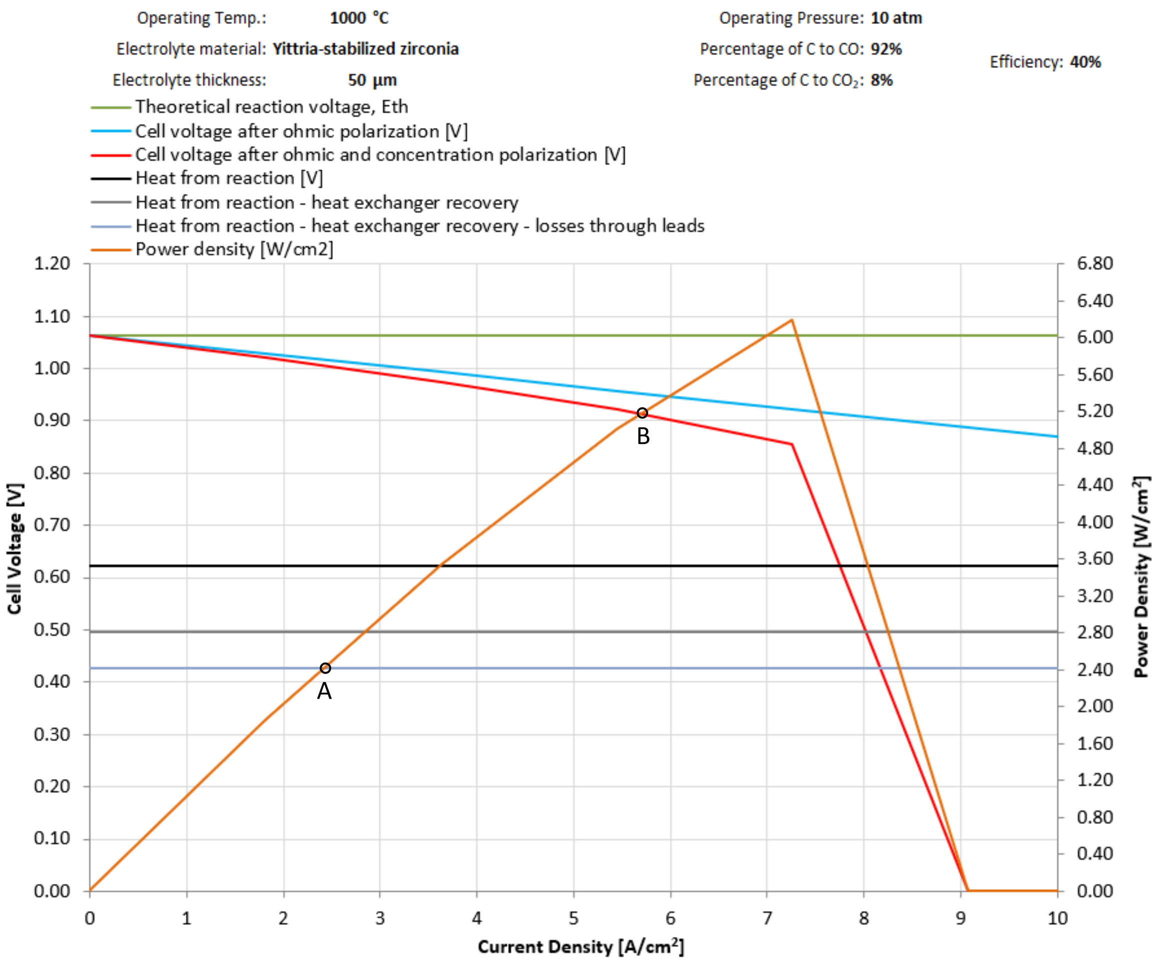

Figure 33: Modified DCFC Evans diagram operating at 1000°C with a maximum operating power density of 5 W/cm^2.

5. Results

5.1 Alloy Compositions After Experiments

Each of the alloys listed in Table 2 were tested in the HT apparatus, with an additional alloy containing a high Sn content melted in-situ. Alloy ingots were reduced to segments of approximately 1cm^3 and packed around the YSZ tubes, shown in **figure 34**, to promote alloy melting and even heat distribution around the electrolyte.

Figure 34: Left: Overall apparatus before starting experiment. Right: close-up of alloy segments in crucible.

All alloys exhibited melting except alloy 4, despite holding this alloy at the maximum furnace controller temperature of 1170°C for 1 hr. Pictures of each alloy are shown in **figure 35**. Alloy compositions after each trial were analyzed again via EDS, with the values listed in **Table 5**. Temperature of the controller and inner and outer thermocouples was recorded at 20-minute intervals during ramp up to 950°C, after which it was recorded every 10 minutes along with voltage measurements using a handheld voltmeter.

Figure 35: Condition of alloys after OCV experiments.

Table 5: Alloy compositions measured via EDS after experiments. Experiments were carried out in alumina crucibles, responsible for the small percentage of aluminum signatures obtained.

Alloy Number	Alloy System	Data Point	Measured Composition [wt. %] via EDS								Measured C [wt. %] via LECO
			Fe	Mn	Ni	Sn	Mo	Si	C	Other	
1	Fe-Mn-Mo-C	1	55.8	9.8			18.2	0.8	8.6	6.9	
		2	47.9	8			33.9	1.5	8.7	0	
		3	72.1	13.4			6.4	0	8.1	0	
		Avg.	58.6	10.4			19.5	0.8	8.5	2.3	
2	Fe-Mn-Sn-C	1	29.9	30.9		32.4		0	4.3	2.6	
		2	28.1	31.6		30.5		0	5.3	0	
		3	38.3	28.3		25.4		1.1	4.3	2.7	
		Avg.	32.1	30.3		29.4		0.4	4.6	1.8	
3	Fe-Mn-Ni-C	1	20.5	36	37.9			2	3.6		3.59
		2	32.3	39.2	22.8			0	5.7		
		3	25.4	32.3	38.9			0.7	2.7		
		Avg.	26.1	35.8	33.2			0.9	4.0		
4	Fe-Mn-Si-C	1	10.5	77.1				7.6	4.8		
		2	11.7	76.2				7.5	4.6		
		3	12.3	73.7				8.4	5.5		
		Avg.	11.5	75.7				7.8	5.0		
5	Fe-Mn-Sn-C	1	21	24.9		48.8		0	2.4	2.9	
		2	13.4	22		58.8		0	1.9	4	
		3	46.5	18.1		31.4		1.9	2.1	0	
		Avg.	27.0	21.7		46.3		0.6	2.1	2.3	

5.2 Open-Circuit Voltage (OCV) Measurements

Voltages from each experiment are presented in **figure 36**. The temperature range in which voltage values could be obtained had a lower limit of 965°C, the melting point of the Ag current collector, and an upper limit of 1170°C, the maximum temperature of the furnace used. These corresponded to internal temperatures of 920°C and 1135°C, respectively.

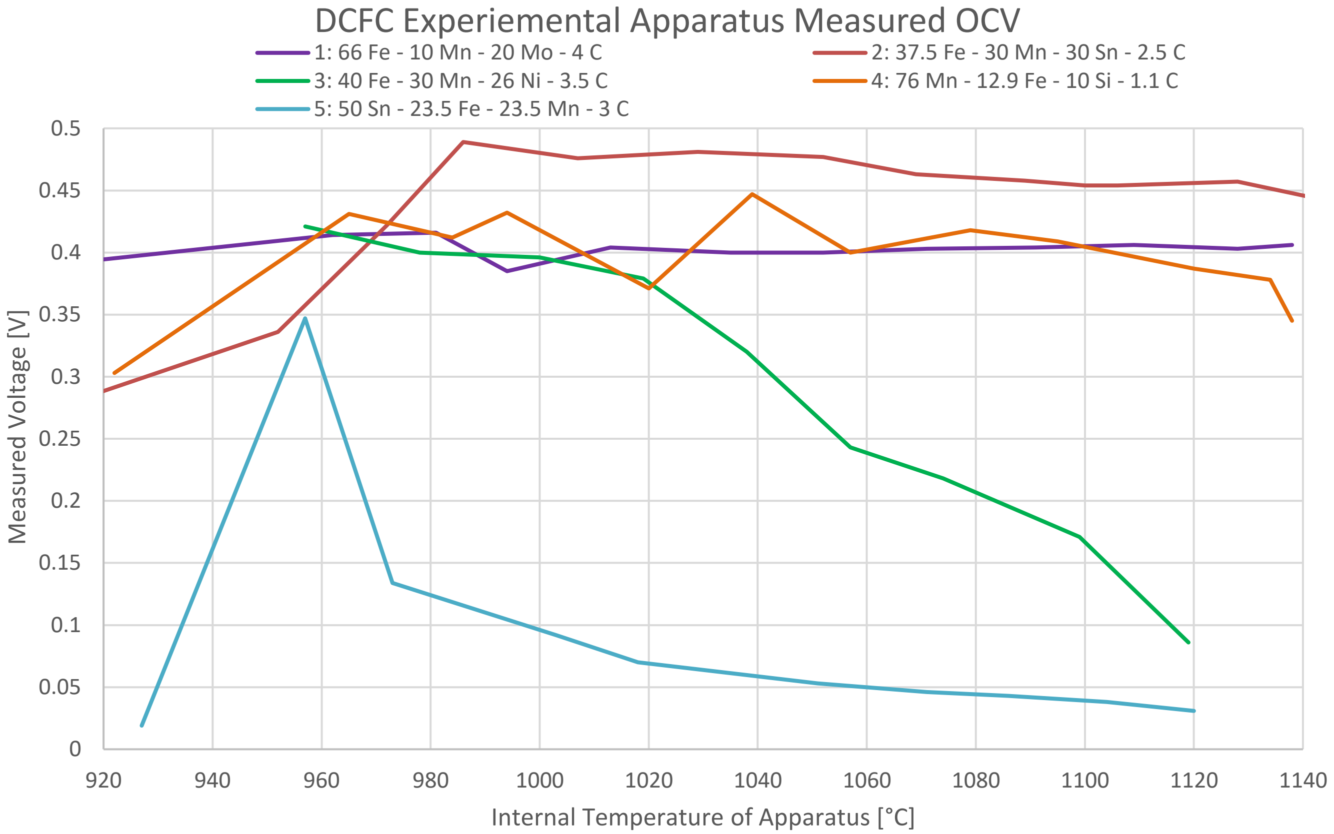

Figure 36: Comparison of OCV measurements from high temperature experimental apparatus as temperature increased from 920°C to 1140°C at a rate of 2°C/min.

Alloy 1 exhibited a stable voltage around 0.4 V throughout the temperature range. Alloy 2 showed the highest voltage measurement of 0.489 V, pictured in **figure 37**, with this value decreasing 9% to 0.445 V at a maximum apparatus temperature of 1141°C. Alloy 3 showed an initial voltage of 0.421 V but decreased to 0.086 V at a maximum temperature of 1119°C. Alloy 4 showed a relatively constant voltage of 0.4 V until the maximum furnace temperature was reached when it decreased to 0.171 V after 80 minutes. Alloy 5 had an initial voltage measurement of 0.35 V but quickly decreased to below 0.1 V where it remained for the rest of the experiment. Apart from alloy 4, all trials revealed the highest voltage readings at or near the initial recording point between 920°C and 950°C.

Figure 37: Maximum voltage of 0.489 V obtained using alloy 2 (37.5 Fe – 30 Mn – 30 Sn – 2.5 C).

All alloys exhibited a decrease in OCV as time increased, with the entire profile for alloy 2 shown as an example in **figure 38**. Potential causes for this behavior are addressed in the following chapter.

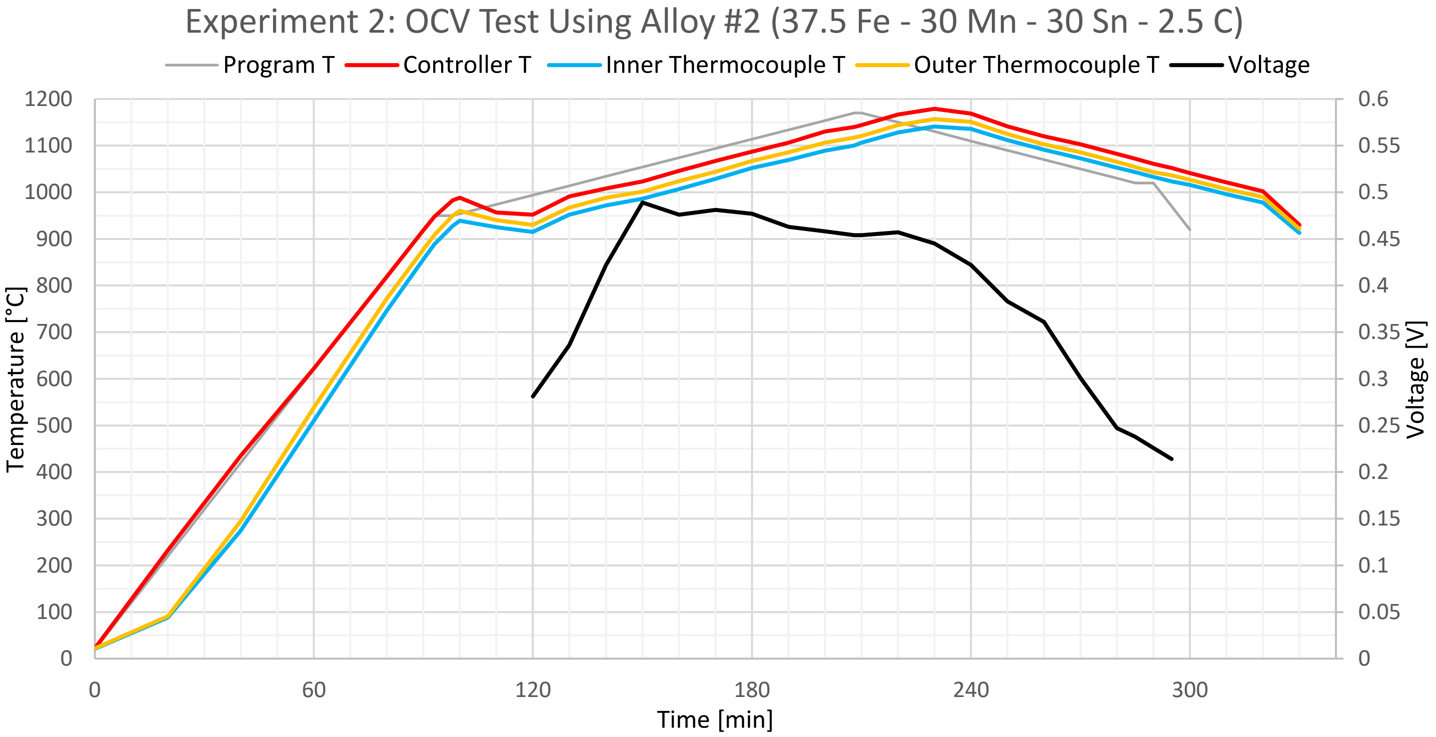

Figure 38: Thermal and OCV measurements from alloy 2. The grey line shows typical temperature profile as programmed into furnace controller for each experiment. Temperature measurements from the inner and outer thermocouples showed values corresponding to 97% and 98% of the controller temperature respectively.

6. Discussion

6.1 Carbon Fuel Phase

Considering the work of Nürnberger et al., it is possible the graphite fuel rod used contributed to the low voltage readings due to the activation energy required to dissolve its crystalline structure. This also could contribute to slow carbon dissolution rate into the alloy, resulting in a decrease in voltage as each trial progressed. Future work could include trials using an amorphous fuel such as carbon black to better understand the effects of fuel type on the performance of this liquid anode DCFC.

6.2 Oxide Formation

Figure 39 shows an oxide layer at the electrolyte surface in a sample cut from alloy 2 after running the experiment. This image reveals that oxides can form on the electrolyte surface in this DCFC. Although it was not observed in other alloy samples, it may contribute to the reduction of OCV measurements as time increased.

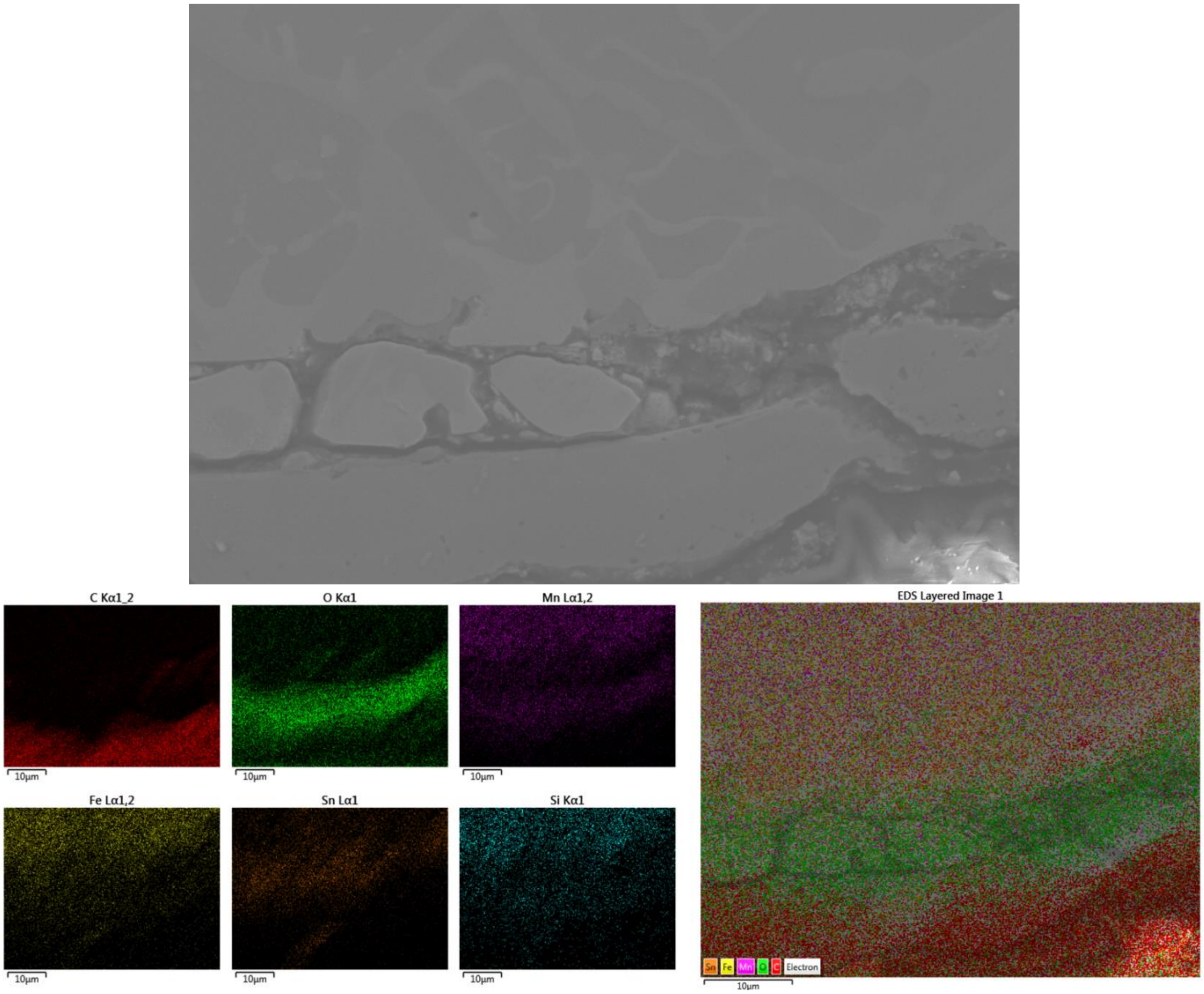

Figure 39: Top: photo of oxide layer at the interface between the anode alloy and electrolyte surface. Bottom: EDS results showing individual species (left) and a composite image (right) with oxide layer in green.

6.3 Experimental Apparatus Limitations

From DSC results, alloy 4 showed a melting temperature upon heating around 1150°C and 1050°C upon cooling. Maximum apparatus temperature was recorded at 1138°C during this trial and therefore could not achieve the temperature required to melt this alloy. Despite this, OCV measurements are considered accurate for the alloy in liquid phase as the other trials did not reveal a significant change in voltage readings as their phase changed from liquid to solid.

EDS did not reveal a significant change in carbon content of alloy samples during the trials. Due to the amorphous nature of the liquid alloy, it is assumed that the samples examined represented the composition of the bulk alloy.

7. Conclusion

This work examined the performance and operation of a novel fuel cell design using a liquid anode alloy. The benefits of this design include: the ability to continuously supply fuel to the electrolyte surface from a variety of carbonaceous solid fuels, capacity for intermittent power generation to supplement renewable sources during peak electricity demand, and high purity of exhaust gases produced which can be easily collected.

Using CALPHAD in conjunction with a literature review, four alloy candidates were chosen based on their thermodynamic and chemical properties. Compared to the Fe-C eutectic, this investigation resulted in the discovery of an alloy composition that reduced of melting temperature by 150°C while still retaining 80% carbon solubility.

Each alloy was melted then tested in a high-temperature electrochemical apparatus. The results showed a peak voltage efficiency of 46%. This low voltage efficiency is attributed to formation of oxides and slow dissolution of the graphite phase in the liquid anode. Higher voltage measurements at lower temperatures and difficulty melting some alloys underscored the need for the anode alloy to have a low liquidus temperature. It is also important that the dissolution rate of carbon within the alloy is high enough to allow carbon to be delivered to the reaction site faster than CO/CO_2 is produced.

7.1 Future Work

Future work could investigate the influence of fuel types (e.g. amorphous vs. crystalline carbon) on apparatus performance. It is anticipated that the implementation of a cathode-supported electrolyte tube will allow for voltage measurements to be taken at lower temperatures as the apparatus will not be limited by the melting temperature of the Ag current collector used in these experiments.

The liquid anode alloy could be further refined via high-throughput calculations to determine a lower liquidus temperature. From the results obtained here, OCV measurements did not show lower values using alloys with low (~2.5 wt.%) carbon solubility. This means the focus of anode alloy development could be primarily on liquidus temperature alone rather than trying to maintain high carbon solubility as well.

Mass and energy balance models were created and show the potential of this device to convert carbon from biomass to electricity at an efficiency of 66%. However in order to achieve this the anode alloy needs to be optimized further requiring its liquidus temperature to be reduced by another 200°C. Additionally more trials need to be conducted to better understand the effects of certain alloying elements, such as Ni and Si on the electrolyte surface and whether or not they form oxide layers that act as a barrier to oxygen ion conductivity.

As global electricity consumption increases in the coming decades, advancements in power generation using carbon-rich solid fuels are required to work with renewable sources of generation to satisfy demand during peak hours. This DCFC design incorporates of over a century of research in electrochemistry, materials science, and metallurgy to answer this challenge, and has the potential to convert solid carbon fuel to electricity at over 1.5x the efficiency of conventional methods.

References

Ahmad, T. and Zhang, D., 2020. A critical review of comparative global historical energy consumption and future demand: The Story Told So Far. *Energy Reports*, Volume 6, pp.1973-1991.

Balmer, R.T., 2011. Second Law of Thermodynamics and Entropy Transport and Production Mechanisms. *Modern Engineering Thermodynamics.* Academic Press. p 214.

BP, 2020. BP Statistical Review of World Energy June 2020. Retrieved from: https://www.bp.com/en/global/corporate/energy-economics/statistical-review-of-world-energy.html

Cherepy, N.J., Krueger, R., Fiet, K.J., Jankowski, A.F. and Cooper, J.F., 2004. Direct conversion of carbon fuels in a molten carbonate fuel cell. *Journal of the Electrochemical Society*, *152*(1), p.A80.

Dong, K., Dong, X. and Jiang, Q., 2020. How renewable energy consumption lower global CO_2 emissions? Evidence from countries with different income levels. *The World Economy*, Volume 43, Issue 6, pp.1665-1698.

Elsayed, Y., Dalibalta, S. and Abu-Farha, N., 2016. Chemical analysis and potential health risks of hookah charcoal. *Science of the Total Environment*, *569*, pp.262-268.

EPA, 2017. Carbon Dioxide Capture and Sequestration: Overview. Retrieved from: https://19january2017snapshot.epa.gov/climatechange/carbon-dioxide-capture-and-sequestration-overview_.html

Filzwieser, A., Hein, K. and Mori, G., 2002. Current density limitation and diffusion boundary layer calculation using CFD method. *JOM*, *54*(4), pp.28-31.

GE, 2016. Breaking the Power Plant Efficiency Record: GE & EDF unveil game-changer at Bouchain. Retrieved from: https://www.ge.com/power/about/insights/articles/2016/04/power-plant-efficiency-record

GE, 2017. HA technology now available at industry-first 64 percent efficiency. Retrieved from: https://www.ge.com/news/press-releases/ha-technology-now-available-industry-first-64-percent-efficiency

Giddey, S., Badwal, S.P.S., Kulkarni, A. and Munnings, C., 2012. A comprehensive review of direct carbon fuel cell technology. *Progress in Energy and Combustion Science*, *38*(3), pp.360-399.

Gillespie, L.K. ed., 1988. *Troubleshooting Manufacturing Processes: Adapted from the Tool and Manufacturing Engineers Handbook: A Reference Book for Manufacturing Engineers, Managers, and Technicians*. Society of Manufacturing Engineers.

Gómez-Acebo, T., Sarasola, M. and Castro, F., 2003. Systematic search of low melting point alloys in the Fe–Cr–Mn–Mo–C system. *Calphad*, *27*(3), pp.325-334.

Gonzales, V., Krupnick, A., and Dunlap, L., 2020. Carbon Capture and Storage 101. Resources for the Future. 6 May. Retrieved from: https://www.rff.org/publications/explainers/carbon-capture-and-storage101/#:~:text=of%20CCS%20technologies.-,The%20State%20of%20CCS,tons%20of%20CO%E2%82%82%20in%202018).

Goret, J. and Tremillon, B., 1967. Propriétés chimiques et électrochimiques en solution dans les hydroxydes alcalins fondus—IV. Comportement électrochimique de quelques métaux utilisés comme électrodes indicatrices. *Electrochimica Acta*, *12*(8), pp.1065-1083.

Green, M. and Ekblom, J., 2018. Investors step up pressure on global energy watchdog over climate change. Reuters, 18 November. Retrieved from: https://news.trust.org/item/20191118073049-nsxvm/

Grove, WR. On voltaic series and the combination of gases by platinum. Philosophical Magazine and Journal of Science. 1839. Issue 14, pp.127-130.

Gu, H., Ran, R., Zhou, W. and Shao, Z., 2007. Anode-supported ScSZ-electrolyte SOFC with whole cell materials from combined EDTA–citrate complexing synthesis process. *Journal of Power Sources*, 2. pp.704-712.

Guo, L., Calo, J.M., DiCocco, E. and Bain, E.J., 2013. Development of a low temperature, molten hydroxide direct carbon fuel cell. *Energy & fuels*, *27*(3), pp.1712-1719.

Hoel, E. G. 1995. Phase Relations of Mn-Fe-Si-C Systems. *INFACON 7*; FFF: Trondheim, Norway. pp 601–610.

Holz, L.I.V., 2017. Zircónia estabilizada com ítria com coloração bege. Departamento de Engenharia de Materiais e Cerâmica. Universidade de Aveiro, pp.14.

Hoste, G., Dvorak, M. and Jacobson, M.Z., 2009. Matching hourly and peak demand by combining different renewable energy sources. *Sanford University, Department of Civil and Environmental Engineering*.

Jacques WW. Method of converting potential energy of carbon into electrical energy. U. S. patent no. 555,1896.

Jayakumar, A., Vohs, J.M. and Gorte, R.J., 2010. Molten-metal electrodes for solid oxide fuel cells. *Industrial & Engineering Chemistry Research*, *49*(21), pp.10237-10241.

Jiang, C., Ma, J., Bonaccorso, A.D. and Irvine, J.T., 2012. Demonstration of high power, direct conversion of waste-derived carbon in a hybrid direct carbon fuel cell. *Energy & Environmental Science*, *5*(5), pp.6973-6980.

Johnstone, N., Managi, S., Rodríguez, M.C., Haščič, I., Fujii, H. and Souchier, M., 2017. Environmental Policy Design, Innovation and Efficiency Gains in Electricity Generation. *Energy Economics*, Volume 63, pp.106-115.

Kakaç, S., Pramuanjaroenkij, A. and Zhou, X.Y., 2007. A review of numerical modeling of solid oxide fuel cells. *International journal of hydrogen energy*, *32*(7), pp.761-786.

Kim, H.S., Kim, D.H. and Hur, T., 2021. Life Cycle Assessment of Molten Carbonate Fuel Cell System for Power Plants. *Journal of Cleaner Production*, Volume 302.

Li, L., Totton, T. and Frenkel, D., 2017. Computational methodology for solubility prediction: Application to the sparingly soluble solutes. *The Journal of chemical physics*, *146*(21), p.214110.

Lin, Z., Lan, X., Xiong, X. and Hu, R., 2021. Recent development of Sn–Fe-based materials as a substitute for Sn–Co–C anodes in Li-ion batteries: a review. *Materials Chemistry Frontiers*.

Lindeburg, M.R., 2020. Mechanical Engineering Reference Manual for the PE Exam, Fourteenth Edition. Kaplan, Inc. pp.29-1-29-3.

Masiá, A.T., Buhre, B.J.P., Gupta, R.P. and Wall, T.F., 2007. Characterizing ash of biomass and waste. *Fuel Processing Technology*, *88*(11-12), pp.1071-1081.

Minh, N.Q., 2004. SOFC technology—features and applications. *Solid State Ionics*, *174*(1-4), pp.271-277.

Nanda, S., Reddy, S.N., Mitra, S.K. and Kozinski, J.A., 2016. The progressive routes for carbon capture and sequestration. *Energy Science & Engineering*, Volume 4, Issue 2. pp.99-122.

Nürnberger, S., Bußar, R., Desclaux, P., Franke, B., Rzepka, M. and Stimming, U., 2010. Direct carbon conversion in a SOFC-system with a non-porous anode. *Energy & Environmental Science*, *3*(1), pp.150-153.

O'Connor, J.J., and Robertson, E.F., 2000. Rudolph Julius Emmanuel Clausius. Retrieved from: https://mathshistory.standrews.ac.uk/Biographies/Clausius/#:~:text=The%20First%20Law%20of%20Thermodynamics,but%20from%20those%20of%20Joule.

Outka, U., 2021. Renewable Energy Siting for the Critical Decade. *Kansas Law Review, Forthcoming*.

Patton, E.M. and Zecevic, S., 2005. Assessment of direct carbon fuel cells. *EPRI report*, *1011496*.

Pati, S., 2010. *Analysis of solid oxide membrane (SOM) electrolyzer with liquid metal anode*. Boston University.
Sinha, A., Shahbaz, M. and Balsalobre, D., 2017. Exploring the Relationship Between Energy Usage Segregation and Environmental Degradation in N-11 Countries. *Journal of Cleaner Production*, Volume 168, Issue 1, pp.1217-1229.

Perez, N., 2004. Kinetics of Concentration Polarization. *Electrochemistry and corrosion science*. Boston: Kluwer academic publishers, pp. 121-154.

Porter, D.A., Easterling, K.E., and Sherif, M.Y.,2009. Phase Transformations in Metals and Alloys. Third Ed. CRC press. p.33.

Powell, A.C., 2010. Minimum Energy Loss Through a High-Temperature Electrolysis Lead. Unpublished.

Sirignano, W.A., and Liu, F., 1999. Performance Increases for Gas-Turbine Engines Through Combustion Inside the Turbine. Journal of Propulsion and Power, Volume 15, Issue 1, pp.111-118.

Stolten, D. ed., 2010. *Hydrogen and fuel cells: fundamentals, technologies and applications*. John Wiley & Sons.

Tanimoto, K., Yanagida, M., Kojima, T., Tamiya, Y., Matsumoto, H. and Miyazaki, Y., 1998. Long-term operation of small-sized single molten carbonate fuel cells. *Journal of power sources*, *72*(1), pp.77-82.

Tao, T., Bateman, L., Bentley, J. and Slaney, M., 2007. Liquid tin anode solid oxide fuel cell for direct carbonaceous fuel conversion. *Ecs Transactions*, *5*(1), pp.463-472.

Thermo-Calc, 2021. CALPHAD Methodology. Retrieved from: https://thermocalc.com/about-us/methodology/the-calphad-methodology/

U.S. Geological Survey (USGS), 2021. Mineral Commodity Summaries 2021. Reston, Virginia. pp. 144, 186.

Velling, A., 2020. Iron-Carbon Phase Diagram Explained. Retrieved from: https://fractory.com/iron-carbon-phase-diagram/

Watanabe, T., Kitamura, S. and Karashima, S., 1980. Grain boundary hardening and segregation in alpha Iron-Tin alloy. *Acta Metallurgica*, *28*(4), pp.455-463.

Yentekakis, I.V., Debenedetti, P.G., Costa, B., Konsolakis, M. and Kiousis, V., 1999. Direct coal gasification with simultaneous production of electricity in a novel fused metal anode SOFC: a theoretical approach. *Ionics*, *5*(5), pp.460-471.

Yoon, K.J., Huang, W., Ye, G., Gopalan, S., Pal, U.B. and Seccombe Jr, D.A., 2007. Electrochemical performance of solid oxide fuel cells manufactured by single step co-firing process. *Journal of the Electrochemical Society*, *154*(4), p.B389-B395.

Zecevic, S., Patton, E.M. and Parhami, P., 2004. Carbon–air fuel cell without a reforming process. *Carbon*, *42*(10), pp.1983-1993.